



Master's Thesis

Through-the-wall UWB Radar Imaging

By

Asif Iqbal & Shabraiz Muhammad

Advisors: Johan Kåredal & Carl Gustafson

Examiner: Fredrik Tufvesson

July, 2011

Department of Electrical and Information Technology

Faculty of Engineering, LTH, Lund University

SE-221 00 Lund, Sweden

Abstract

The focus of this master's thesis project is to use the Ultra Wideband signals to locate target objects behind a wall. It also includes the comparison of two migration algorithms used for generating the 2-D images of the environment. The thesis is done at the department of Electrical & Information Technology, LTH, Lund University, Sweden. The ability to see beyond a wall or any obstacle could find its use in several applications among the fields of security, disaster management etc.

The ability of Ultra Wideband signals in penetrating the wall is exploited to get information about the environment unseen by the human eye i.e. beyond an obstacle. The time resolution of UWB signals, being very high, allows us to get a range resolution up to few centimeters. Consequently, the dimensions of the targets can also be found. The measurements are done in the frequency domain in the frequency range of 9.0 to 16.5 GHz using Vivaldi antennas. Synthetic Aperture Radar technique is used for the measurements.

The migration algorithms selected for the task are Phase-Shift method (using scalar wave equation) and Diffraction Stack algorithm (using geometrical approach). Both algorithms give good accuracy about the location of the targets, but the Phase-Shift method is chosen as the better one due to its faster execution time, extracting higher detail about the environment due to lower side lobe levels in the resulting 2-D image as compared to Diffraction Stack algorithm.

Acknowledgement

First and foremost, we would like to thank Allah, subhana wa ta'ala, for endowing us with health, patience and knowledge to complete this thesis work.

We would like to thank our parents who brought us into this world and supported us to acquire such profound knowledge and excellence. They encouraged us by putting their confidence in us so that we could make grave decisions of our lives related to our academic careers and professional expertise.

We owe our deepest gratitude to our supervisors, Dr. Johan Kåredal for his guidance, encouragement and support during the initial research phase of the thesis, and Carl Gustafson for his technical advices, assistance in performing measurements, and guidance during the report writing phase. We would like to thank our examiner Dr. Fredrik Tufvesson for his guidance and support throughout the thesis.

We would also like to thank our seniors, especially Taimoor Abbas and Muhammad Atif Yaqoob for helping us whenever we needed it the most.

Heartiest thanks go to all our colleagues for their friendship and support throughout the thesis work.

List of Figures

Figure 1.1.1: Penetration Loss through a 12 cm thick slightly reinforced non-uniform concrete wall	2
Figure 2.2.1: Basic UWB Radar Principle	6
Figure 2.3.1: a) 2D SAR spatial Model. b) B-scan of the point	7
Figure 2.5.1: Electromagnetic wave propagating through the wall	10
Figure 2.7.1: Discrete Fourier Transform pair	16
Figure 3.1.1: a) Synthetic Aperture Radar	19
Figure 3.1.2: Spatial model of wave penetrating through the wall	21
Figure 3.1.3: Differential SAR model	22
Figure 3.1.4: a) ERM with wave field originating at target surface at $t = 0$ and propagating with half speed. b) Wave field leaving transmitter, gets reflected from the target surface and is received by the receiver.	23
Figure 3.1.5: A multi-static Antenna configuration	25
Figure 4.1.1: Point Scatterer located at 1 meter away from center of the antenna aperture	30
Figure 4.1.2: B-scan $B(X, k = TOA)$	31
Figure 4.2.1: Theoretical beam pattern obtained by diffraction stack and Phase Shift method for a) $\Delta f = 5$ MHz and $\Delta x = 1$ cm, and b) $\Delta f = 10$ MHz and $\Delta x = 2$ cm	32
Figure 4.2.2: Numerical simulation of distributed targets. a) image obtained by Diffraction Stack algorithm, b) image obtained by Phase-Shift Method.	34
Figure 4.2.3: Closely placed point targets	35
Figure 4.2.4: Synthetic Impulse Response	35
Figure 4.2.5: Migrated Image by Phase-Shift Migration	35
Figure 5.1.1: Block Diagram of UWB Radar System	38
Figure 5.1.2: Vivaldi Antenna with a coaxial connector	40
Figure 5.1.3: Trolley with Tx and Rx antennas	41
Figure 5.1.4: UWB Radar System Overview	42
Figure 5.3.1: Range and Cross-Range Resolution	45
Figure 5.3.2: 2D Image Resolution	46
Figure 5.3.3: PS results for scenario 3 with a) $\Delta x = 6$ cm, and b) $\Delta x = 2$ cm	48
Figure 5.4.1: S_{21} for a single antenna position	49
Figure 5.4.2: a) Cable Attenuation b) LNA Gain	50
Figure 5.4.3: Impulse response of Unprocessed SAR data	51
Figure 5.4.4: Impulse Response after 20 meter long cable's effect removal	51

Figure 5.4.5: Impulse response after full calibration	52
Figure 5.4.6: Transfer Function after data correction	52
Figure 5.4.7: Transfer function without direct antenna component.....	53
Figure 6.0.1: Target Objects for Scenario 1 & 2	56
Figure 6.1.1: Measurement Scenario 1 Layout	57
Figure 6.1.2: a) Imaging results from Phase-Shift Algorithm, b) Diffraction Stack Algorithm.....	58
Figure 6.2.1: Cylinder in front of Plate in Scenario 2.....	59
Figure 6.2.2: Measurement Scenario 2 layout.....	60
Figure 6.2.3: a) Image generated by Phase-Shift Algorithm, b) Image generated by Diffraction Stack Algorithm.....	61
Figure 6.3.1: Metallic Plate and the cylinder placed in two different rooms	62
Figure 6.3.2: a) Antenna Assembly, b) & c) 9 meter long rail covering 3 offices, along with the VNA and Laptop, d) wooden cabinet with two bottles inside room 1	63
Figure 6.3.3: Scenario 3 Layout	64
Figure 6.3.4: Scenario 3-without wall compensation	65
Figure 6.3.5: Wall Compensated Images. a) Image Generated by Phase-Shift Method b) Image Generated by Diffraction Stack.....	67
Figure 6.4.1: Practical Resolution using full 9 – 16.5 GHz	70
Figure 6.4.2: Practical Resolution using 9 – 12.5 GHz.....	71
Figure 6.4.3: Practical Resolution using 12.5 – 16.5 GHz.....	72
Figure 6.4.4: DS results for Scenario 1 using different frequency ranges	74
Figure 6.4.5: PS results for Scenario 1 using different frequency ranges	75
Figure 6.4.6: DS results for Scenario 2 using different frequency ranges	76
Figure 6.4.7: PS results for Scenario 2 using different frequency ranges	77
Figure 6.4.8: DS results for Scenario 3 using different frequency ranges	78
Figure 6.4.9: PS results for Scenario 3 using different frequency ranges	79
Figure A.1: $\epsilon_r = 4.5$, $Lw = 12\text{ cm}$	84
Figure A.2: $\epsilon_r = 4.95$, $Lw = 12\text{ cm}$	85
Figure A.3: $\epsilon_r = 2.83$, $Lw = 4\text{ cm}$	86

Table of Contents

ABSTRACT.....	I
ACKNOWLEDGEMENT.....	II
LIST OF FIGURES	III
TABLE OF CONTENTS	V
CHAPTER 1:.....	1
1. INTRODUCTION.....	1
1.1. ULTRA-WIDEBAND SIGNALS.....	1
1.2. PROBLEM DESCRIPTION.....	2
1.3. THESIS ORGANIZATION.....	3
CHAPTER 2:.....	5
2. ULTRA-WIDEBAND RADAR SYSTEM	5
2.1. CONCEPT OF RADAR.....	5
2.2. UWB RADAR FUNDAMENTALS.....	6
2.3. SYNTHETIC APERTURE RADAR SCANNING	7
2.4. STEPPED FREQUENCY CONTINUOUS WAVE RADAR SYSTEM (SFCW).....	8
2.5. ELECTROMAGNETIC WAVE PENETRATING THROUGH THE WALL	9
2.6. PLANE WAVE EQUATION	11
2.7. FOURIER METHODS	13
2.7.1. CONTINUOUS FOURIER TRANSFORM (FT)	13
2.7.2. DISCRETE FOURIER TRANSFORM (DFT)	14
2.7.3. DFT PARAMETER CALCULATIONS	14
CHAPTER 3:.....	17
3. SYNTHETIC APERTURE RADAR MIGRATION ALGORITHMS	17
3.1. BACK PROJECTION AND BACK PROPAGATION	18
3.1.1. BACK PROJECTION ALGORITHMS.....	18
3.1.1.1. <i>Diffraction Stack (TOA Estimation)</i>	18
3.1.1.2. <i>Simple Wall Compensation</i>	20

3.1.1.3.	<i>Differential SAR</i>	21
3.1.2.	BACK PROPAGATION ALGORITHMS.....	22
3.1.2.1.	<i>Exploding Reflector Model (ERM)</i>	22
3.1.2.2.	<i>Kirchhoff Migration</i>	24
3.1.2.3.	<i>Phase-Shift Migration (F-K)</i>	26
CHAPTER 4:	29
4.	SELECTION OF ALGORITHMS AND ANALYSIS	29
4.1.	SYNTHETIC DATA GENERATION.....	29
4.2.	COMPARISON OF MIGRATION METHODS.....	31
4.2.1.	PERFORMANCE FOR POINT LIKE TARGET.....	31
4.2.2.	PERFORMANCE FOR CLOSELY-PLACED TARGETS.....	33
CHAPTER 5:	37
5.	UWB RADAR DEVICES AND SETUP	37
5.1.	UWB RADAR SYSTEM DESIGN.....	37
5.1.1.	VECTOR NETWORK ANALYZER (VNA).....	37
5.1.2.	ANTENNA SELECTION.....	40
5.1.3.	DEVICES CONNECTION SETUP.....	41
5.2.	CHANNEL MEASUREMENTS.....	42
5.3.	SYSTEM PARAMETERS.....	43
5.3.1.	SELECTED BANDWIDTH.....	43
5.3.2.	FREQUENCY STEP INTERVAL Δf	44
5.3.3.	CROSS RANGE SAMPLE INTERVAL Δx	44
5.3.4.	DOWN-RANGE RESOLUTION δz	44
5.3.5.	CROSS-RANGE RESOLUTION δx	45
5.3.6.	RADAR SYSTEM LIMITS.....	46
5.4.	SIGNAL PROCESSING STEPS.....	48
5.4.1.	RECEIVED TRANSFER FUNCTION.....	49
5.4.2.	EFFECTS OF CABLES AND LNA.....	49
5.4.3.	DATA CORRECTION.....	50
CHAPTER 6:	55
6.	EXPERIMENTAL SCENARIOS & RESULTS	55
6.1.	SCENARIO 1: DESCRIPTION & RESULTS.....	56

6.2.	SCENARIO 2: DESCRIPTION & RESULTS.....	59
6.3.	SCENARIO 3: DESCRIPTION & RESULTS.....	62
6.3.1.	RESULTS WITHOUT WALL COMPENSATION	64
6.3.2.	RESULTS WITH WALL COMPENSATION.....	66
6.4.	RESULTS FOR SMALL BANDWIDTH	68
	CHAPTER 7:.....	81
7.	CONCLUSIONS & FUTURE WORK.....	81
7.1.	CONCLUSIONS.....	81
7.2.	FUTURE WORK	82
	APPENDIX.....	83
A.	RESULTS WITH DIFFERENT ϵ_r AND WALL WIDTH.....	83
	REFERENCES	87

Chapter 1:

1. Introduction

1.1. Ultra-Wideband Signals

The bandwidth of a signal is the measure of the frequency content it has. Based on this criteria, the signals can be narrowband, wideband, or ultra-wideband. Signals having a bandwidth greater than 500 MHz or greater than 20% of the carrier frequency are characterized as Ultra-Wideband signals. Due to such large bandwidth, UWB signals have a very fine time resolution [1], as seen in eq. (1.1), thus being ideal for precision ranging and tracking applications. These signals can be generated as very short pulses or by simultaneous transmission over a large bandwidth. UWB signals have very low power over the band and thus don't add to the interference level of existing communication services. Also due to their large bandwidth, UWB signals are very difficult to jam.

$$\delta t = 1/B \quad (1.1)$$

δt is the smallest unit of time under which the channel can be viewed and B is the bandwidth used to measure the channel.

Federal Communication Commission (FCC), in 2002, allocated frequency band of 3.1 GHz to 10.6 GHz as unlicensed band with a bandwidth of 7.5 GHz for the general public, as a result, this band is mostly used by various systems and UWB applications for achieving fast-rate communications and precision ranging among other applications. As UWB signals, having frequencies from 3 to 4 GHz [2], [18] are able to pass through concrete walls without high attenuation, so, the range of 3.1 to 10.6 GHz can be effectively used by the UWB radar systems. Penetration loss for this frequency range is shown in figure 1.1.1. [2].

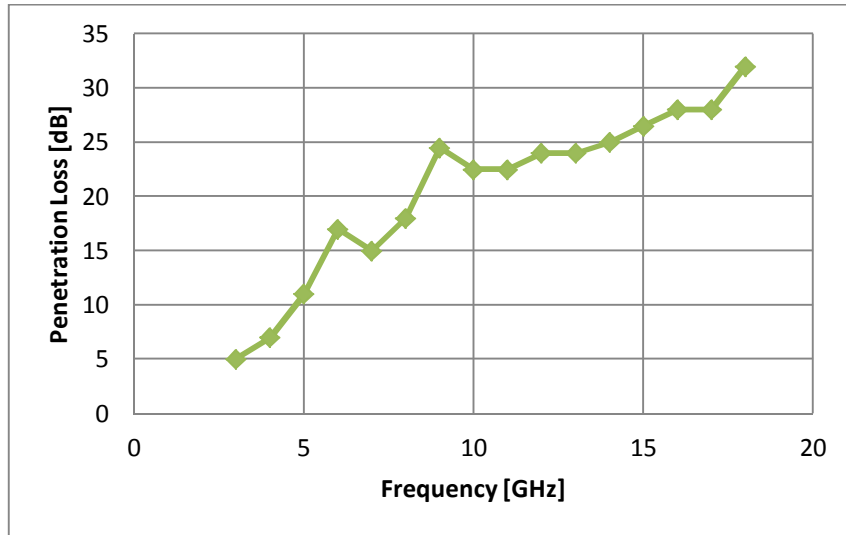


Figure 1.1.: Penetration Loss through a 12 cm thick slightly reinforced non-uniform concrete wall

1.2. Problem Description

The idea is to use a stepped-frequency UWB radar system to scan the environment in front of the antennas and try to identify any targets even if they are behind the wall. The system transmits electromagnetic waves from the transmit antenna, waves pass through the wall, strike the target objects, get reflected back, passing through the wall again and are received at the receive antenna. When passing through the wall, electromagnetic waves suffer absorption, reflection, refraction and diffraction at the boundaries of the wall [3]. All of these phenomena depend upon the properties of the material constituting the wall and the frequency of the EM waves. Ideally, the width of the wall should not be too thick and the material of the wall should be such that the electromagnetic waves can pass through it without much attenuation. Apart from the direct path from the target, there will be many reflections from other objects, walls and floor received by the receiver. Another very important phenomenon is the variation of wave travelling speed while passing through the wall, which depends upon the properties of the wall material.

Due to the above factors, the received signals at the antennas will be complex, noisy and will contain a lot of clutter. At this point, the received data is not in a comprehensible state. Now the main objective of the signal processing steps is to

use the received data and make an image of the environment which is understandable to the end user. There are several methods to accomplish this but they provide varying accuracy.

Radar imaging methods have been in use for a long time and are mainly used in Ground Penetrating Radar (GPR) applications [5], whereas, through-the-wall imaging is relatively new application using these methods [4]. The implementation of most of the GPR imaging methods on practical measurements for through-the-wall imaging do not provide good and precise results, so, there is still a lot of research possibilities in the field of signal processing and radar hardware to make through-the-wall imaging usable in the practical situations.

1.3. Thesis Organization

In chapter 2, Ultra-wideband radar system is discussed along with the UWB radar system fundamentals, effect of wall on the travelling wave, Synthetic Aperture Radar (SAR), stepped frequency radar system, a look at plane wave equation, Fourier methods along with a brief look at the relationship between impulse response and transfer function. In chapter 3, various SAR imaging methods discussed and divided into two main categories explaining each one in detail; important methods include Phase-Shift method and the Diffraction Stack algorithm. In chapter 4, the selected imaging methods, Phase-Shift method and the Diffraction Stack algorithm, are implemented and verified using synthetic data. In chapter 5, UWB radar setup and devices used are discussed including the selected system parameters for the operation of the radar system. Chapter 6 contains imaging results of real measurements based on practical scenarios and their analysis. Finally, the conclusion of this thesis and possible extensions of the work are proposed in chapter 7.

Chapter 2:

2. Ultra-Wideband Radar System

2.1. Concept of Radar

Radar systems are used to detect objects which are beyond the visual range of the naked eye. They transmit electromagnetic waves and then process the received waves to determine the range, velocity (direction and speed) and altitude of the target objects. These objects can be aircraft, ships, ballistic or guided missiles, weather formations (clouds, hurricanes) etc.

Short Pulse Radar systems transmit radio waves in all directions, when these waves come across any object, they are reflected and scattered in various directions. These signals are then received at the receiver of the radar systems, are amplified and processed to get the required information about speed, distance, altitude etc. of the target. As radio waves can travel through the air, fog, clouds etc. without undergoing much attenuation, they can be used to identify targets for relatively long ranges.

As we know that the atmospheric attenuation varies over the frequency of the radio waves with the attenuation increasing with increasing frequency, whereas, the achievable accuracy and range resolution (leading to object identification) is high for signals having higher bandwidth. So there is always a tradeoff between maximum range and maximum resolution of the radar system.

So far we have discussed short pulse radar system; there is another form of radar called Ultra-Wideband (UWB) radar using UWB signals. UWB radar has several advantages over the Short Pulse radar systems, [6], such as

- UWB signals can be transmitted without a carrier and with relatively less power.
- Due to higher bandwidth, UWB radar gives much better target range measurement accuracy.

- Target identification possible as the received signals contain the information about not only the whole target, but also its different parts.
- Less radar effects due to rain, mist, aerosols, metalized strips etc.
- Highly immune to noise, detection, jamming, and narrowband interference from existing radio systems.

2.2. UWB Radar Fundamentals

The basic principle behind UWB radar system is shown in figure 2.2.1. The UWB radar system generates and transmits a short pulse from the transmitting antenna TX, the electromagnetic wave travels through the propagation channel to the target, a part of it is reflected and travels back through the channel reaching receiving antenna RX. The time delay t between the transmission and reception of the signal corresponds to the distance between the antennas and the target according to eq. (2.1). Due to high bandwidth of the signal, we can calculate the distance very precisely. As the wave travels at the speed of light c , the time t can be converted to distance Z by

$$Z = \frac{c * t}{2} \quad (2.1)$$

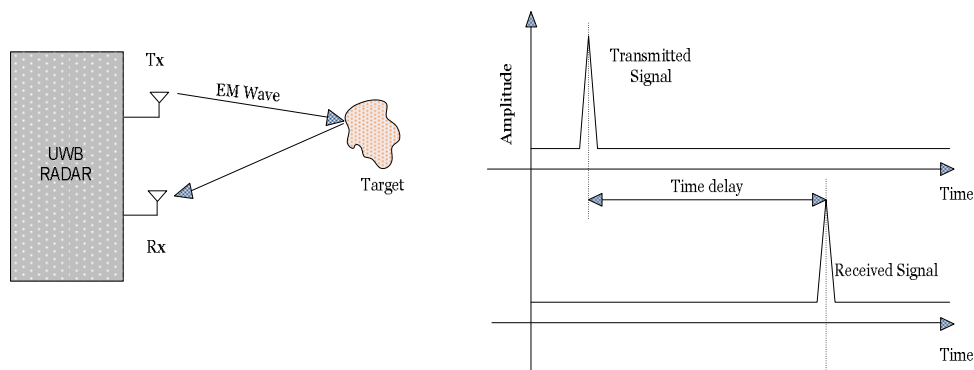


Figure 2.2.: Basic UWB Radar Principle

2.3. Synthetic Aperture Radar Scanning

Synthetic aperture radar (SAR) is a special type of radar which uses the relative motion between antennas and their target, normally moving antennas and a stationary target, to get distinctive signal variations which are used to obtain finer range resolution of the target. This kind of scanning is usually used on airplanes and naval ships where the target area is repetitively illuminated by the beam of the antenna and waves are received coherently along the movement path at different positions simulating a long virtual array.

Transmitting a short pulse and then receiving it at one location gives us the impulse response of the channel for those particular locations and the environment. But in our case, only one impulse response is not enough to locate the target at correct location, so, more information is needed about the investigated object. In order to do that, we used SAR scanning to get the required information about the channel and the target. Basic SAR scanning technique is shown in figure 2.3.1 (a), where X is the scanning direction and Z is the looking direction.

During a complete SAR scan, the entire environment including the target object T is stationary while antennas move along the X direction. Assuming the transmitted wave is reflected by the target uniformly in all directions, and assuming a wide antenna beamwidth, the signal is received not only when the antenna is right below the target, but also at several other antenna positions. This causes the one point in $S(X, Z)$ domain to be seen as a hyperbola in the acquired B-scan $B(X, k)$ as shown in Figure 2.3.1 (b).

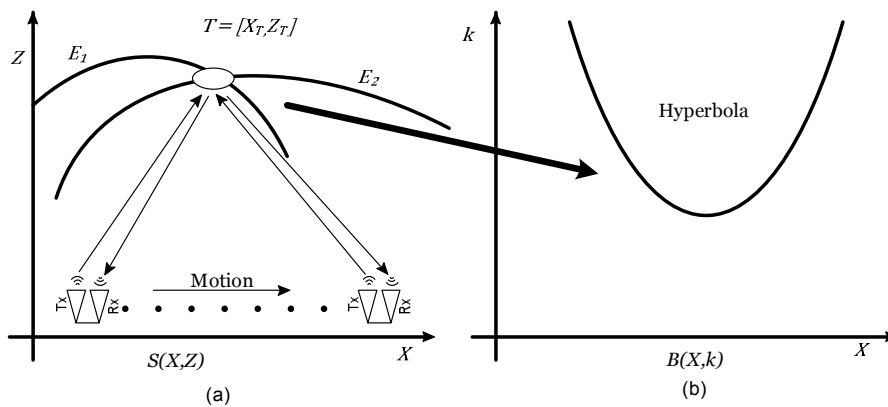


Figure 2.3.: a) 2D SAR spatial Model. b) B-scan of the point

B-scan $B(X, k = TOA_n)$, given in Figure 2.3.1 (b), shows the round trip time (RTT) of the transmitted pulse for the complete synthetic aperture array with k corresponding to the RTT of the received pulse at each antenna position. As seen here, one point in $S(X, Z)$ is seen as a hyperbola in the B-scan $B(X, k)$. E_1 and E_2 correspond to the circles where the target could be located with respect to the antenna positions, corresponding to a single RTT.

2.4. Stepped Frequency Continuous Wave Radar System (SFCW)

UWB radar can work in either time-domain or in the frequency domain. When working in time domain, the transmitter transmits a single very short pulse (less than a few Nano-seconds) and receiving the impulse response of the channel. In order to have a very short pulse, the bandwidth of the signal has to be very high, which results into a fine time resolution. In contrast, UWB radar working in frequency domain emits a series of tones with a specific frequency f Hz with a constant step of Δf Hz from the selected band of frequencies. At each f , the amplitude and phase of the received signal is recorded by a vector network analyzer (VNA).

Figure 2.3.1 (a) shows a SAR spatial scan with an aperture length of X ; we sample the *cross-range* x with the interval of Δx , recording impulse response for each position x_p where $p = 1, \dots, P$, where $P = X/\Delta x + 1$. The temporal response of the channel when transmitting an impulse $\delta(t)$ at $t = 0$ is

$$h(t, x_p, z = 0) = \sum_k a_k \delta(t - t_k) \quad (2.2)$$

The impulse response consists of multipath components indexed through k with t_k denoting the individual time of arrival and a_k representing the complex amplitudes containing information about both amplitudes and phase of the received signals [1]. $z = 0$ in $h(t, x_p, z = 0)$ corresponds to the location of transmit TX and receive RX antennas in the spatial domain $S(X, Z)$.

Corresponding to the above impulse response, the frequency response is given below:

$$H(f, x_p, z = 0) = \sum_k a_k e^{-j2\pi f t_k} \quad (2.3)$$

The frequency response shows us that the channel can be constituted by a frequency scan i.e. sampling $H(f, x_p, z = 0) = \frac{Y(f)}{X(f)}$ with the frequency interval of Δf in the frequency band B and a center frequency f_c transmitting tones $X(f)$ and receiving the channel response $Y(f)$ at the receiver.

The SFCW radar system has some advantages over the time-domain radar system which includes; wider dynamic range, higher mean power, lower noise level and the ability to change the power spectral density [7]. Moreover, the impulse response and the transfer function can be obtained from one another by the help of “Fourier Transform”.

2.5. Electromagnetic Wave Penetrating Through the Wall

As the target of this thesis is to implement a radar system which can see through the wall, and as we will be using electromagnetic waves to get the information about the environment on the other side of the wall, so in order for the electromagnetic waves to give this information, they have to first pass through the wall. The wall could be made up of materials like concrete blocks, clay bricks, metallic rods, dry wall, fiber glass isolation etc. The electromagnetic waves suffer a lot of attenuation during propagation between the transmit antenna, target and back to receive antennas. These losses consist of free-space path loss, scattering and reflection from the surface of the wall, absorption in the wall material and scattering by the target object. We already know that the propagation loss outside as well as inside the wall depends upon the frequency of the transmitted wave field [2]. By using a large enough bandwidth, it is made sure that enough information will be received about the channel.

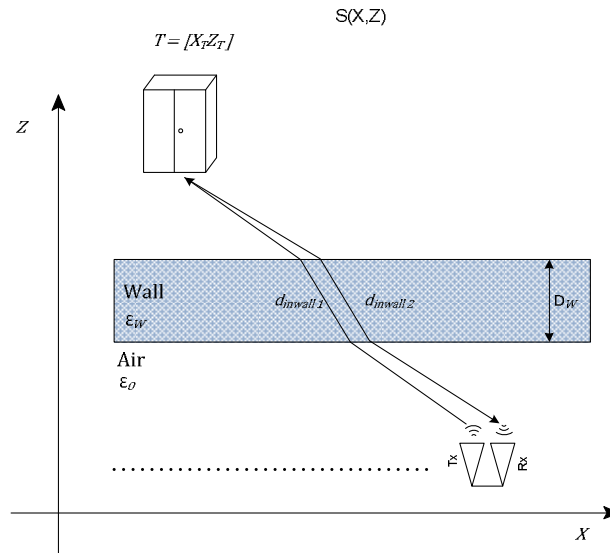


Figure 2.5.: Electromagnetic wave propagating through the wall

When electromagnetic waves reach the surface of the wall at a particular angle, some of it will get reflected while some of its energy will continue to propagate inside the wall but with different speed and angle as seen in figure 2.5.1. This happens because the relative permittivity of the wall ϵ_{rw} is different from the permittivity of the air ϵ_a . As the permittivity of the wall is always greater than that of air $\epsilon_{rw} > \epsilon_a$, the speed of wave will be less than its speed in the air which is c . Assuming a homogeneous wall, the propagation speed inside the wall can be calculated from the formula;

$$V_w = \frac{c}{\sqrt{\epsilon_{rw}}} \quad (2.4)$$

If the ϵ_a in front of the wall is same as ϵ_a behind the wall, then the electromagnetic wave will leave the wall with the same angle with which it entered the wall i.e. the direction will be the same.

2.6. Plane Wave Equation

In order to get to the scalar plane wave equation, we have to start from the very basics of electromagnetic theory [19]; i.e. the Maxwell's equations. Maxwell's equations in the time domain are written as:

$$\nabla \times \vec{E}(\vec{r}, t) = -\frac{\partial}{\partial t} \vec{B}(\vec{r}, t) \quad (2.5)$$

$$\nabla \times \vec{H}(\vec{r}, t) = \vec{J}(\vec{r}, t) + \frac{\partial}{\partial t} \vec{D}(\vec{r}, t) \quad (2.6)$$

$$\nabla \cdot \vec{B}(\vec{r}, t) = 0 \quad (2.7)$$

$$\nabla \cdot \vec{D}(\vec{r}, t) = \rho(\vec{r}, t) \quad (2.8)$$

Where \vec{E} is the electric field intensity, \vec{H} is the magnetic field intensity, \vec{B} is the magnetic flux density, \vec{D} is the electric flux density, \vec{J} is the current density, and ρ is the electric charge density.

These densities are related to the corresponding intensities according to the following relations;

$$\vec{D} = \epsilon \vec{E}, \quad (2.9)$$

$$\vec{B} = \mu \vec{H}, \quad (2.10)$$

$$\vec{J} = \sigma \vec{E}, \quad (2.11)$$

where ϵ , μ , and σ are the properties of the material and are called electric permittivity, magnetic permeability, and conductivity of the medium respectively.

Consider a source-free, linear, homogeneous, and isotropic region of space i.e. having current density and charge density zero ($\vec{J}(\vec{r}, t) = 0$ and $\rho(\vec{r}, t) = 0$). We can write equations (2.5) and (2.6) in frequency domain as:

$$\nabla \times \vec{E} = -\hat{z} \vec{H} \quad (2.12)$$

$$\nabla \times \vec{H} = \hat{y} \vec{E} \quad (2.13)$$

Taking curl of eq. (2.12) and substituting the result into eq. (2.13), we get;

$$\nabla \times \nabla \times \vec{E} - k^2 \vec{E} = 0 \quad (2.14)$$

Eq. (2.14) is called “complex vector wave equation”. Similarly, we can write;

$$\nabla \times \nabla \times \vec{H} - k^2 \vec{H} = 0 \quad (2.15)$$

Where \hat{z} and \hat{y} are impedivity and admitivity of the medium. k is the wavenumber. They are related according to the relation;

$$k = \sqrt{-\hat{z}\hat{y}} \quad (2.16)$$

$$\nabla^2 \vec{A} = \nabla(\nabla \cdot \vec{A}) - \nabla \times \nabla \times \vec{A} \quad (2.17)$$

By using the Laplacian operator given in eq. (2.17) and the taking the divergence of \vec{E} and \vec{H} equal to zero, we get;

$$\nabla^2 \vec{E} + k^2 \vec{E} = 0 \quad (2.18)$$

$$\nabla^2 \vec{H} + k^2 \vec{H} = 0 \quad (2.19)$$

The above equations are called vector wave equations. An interesting thing is that rectangular components of \vec{E} and \vec{H} , both satisfy the “complex scalar wave equation” also called “Helmholtz equation” given by

$$\nabla^2 \psi + k^2 \psi = 0 \quad (2.20)$$

We can replace ψ in eq. (2.20) by any of the rectangular components of \vec{E} and \vec{H} (E_x, E_y, E_z , or H_x, H_y, H_z).

Wave equation in the time domain can be written as

$$\nabla^2 \psi - \mu\epsilon \frac{\partial^2 \psi}{\partial t^2} - \mu\sigma \frac{\partial \psi}{\partial t} = 0 \quad (2.21)$$

Assuming the propagation medium is lossless i.e. $\sigma = 0$ and replacing $1/\mu\epsilon$ by v^2 , which is the velocity of the wave in the medium, we get;

$$\nabla^2 \psi - \frac{1}{v^2} \frac{\partial^2 \psi}{\partial t^2} = 0 \quad (2.22)$$

Consider 2-D wave-field in rectangular coordinates, $\psi(z, x, t)$, we can write the above equation in the terms of $\psi(z, x, t)$ as;

$$\left(\frac{\partial^2}{\partial x^2} + \frac{\partial^2}{\partial z^2} - \frac{1}{v^2} \frac{\partial^2}{\partial t^2} \right) \psi(z, x, t) = 0 \quad (2.23)$$

The above equation is called ‘‘Scalar Wave Equation’’. Use of this equation will be discussed in the later chapters.

2.7. Fourier Methods

Fourier transform is a very useful analysis tool for any signal as it lets us see the signal in more than one domain. For example, a time domain signal $u(t)$ can be decomposed into the individual frequencies which make up the signal, resulting in a frequency domain representation $U(f)$ of the signal.

The signals in real life are all continuous, but in order to study and process them, they are sampled and converted into discrete samples of the signal. Consequently, there are two forms of Fourier transforms;

- i. Continuous time Fourier transform
- ii. Discrete time Fourier transform

2.7.1. Continuous Fourier Transform (FT)

Continuous time Fourier Transform (FT) of a signal $u(m)$ is given by [19]

$$U(k_m) \approx \frac{1}{\sqrt{2\pi}} \int_{-\infty}^{\infty} u(m) e^{-jk_m m} dm \quad (2.24)$$

And the inverse Fourier Transform (IFT) is given by

$$u(m) = \frac{1}{\sqrt{2\pi}} \int_{-\infty}^{\infty} U(f_m) e^{jk_m m} dk_m \quad (2.25)$$

Where k_m is the variable in the Fourier domain. If the variable $m = t$ i.e. time, then $k_m = \omega$, furthermore, if $m = x$ where x is a spatial variable, then $k_m = k_x$ i.e. wave number in the spatial direction x . A negative exponential in the Fourier transform is called forward transform and a positive exponential is the corresponding negative transform.

2.7.2. Discrete Fourier Transform (DFT)

Discrete Fourier Transform (DFT) is used to transform discrete time signals into discrete Fourier domain. DFT is actually an approximation of the continuous time Fourier transform [19].

Assume a discrete signal $u(m)$ consisting of N samples taken with a sampling period of Δm . The resulting Fourier transform expression will be

$$U(k_m) \approx \frac{1}{\sqrt{2\pi}} \int_0^{\Delta m N} u(m) e^{-jk_m m} dm \quad (2.26)$$

And the resulting discrete-time form of Fourier transform will be

$$U(k_m) \approx \frac{1}{\sqrt{2\pi}} \sum_{n=0}^{N-1} u(n\Delta m) e^{-jk_m n\Delta m} \Delta m \quad (2.27)$$

In eq. (2.27), k_m is a continuous variable, so, we will sample it into a set of k_m^p discrete samples with $k_m^p = 2\pi p / ((N-1)\Delta m)$, where $p = 0, 1, \dots, N-1$ and multiplying the transform summation of eq. (2.27) with $\sqrt{2\pi} / (\Delta m)$. The Fourier domain variable k_m is sampled over $-K_{mmax}$ to K_{mmax} [19].

The resulting expression for Discrete Fourier Transform (DFT) is given by

$$U(k_m^p) = \sum_{n=0}^{N-1} u(n\Delta m) e^{-j2\pi p \frac{n}{N}} \quad (2.28)$$

Similarly, Inverse Discrete Fourier Transform (IDFT) is given by

$$u(n\Delta m) = \frac{1}{N} \sum_{n=0}^{N-1} U(k_m^p) e^{j2\pi p \frac{n}{N}} \quad (2.29)$$

To study DFT in full detail, see any standard text book like [16].

2.7.3. DFT Parameter Calculations

As the Phase-Shift migration algorithm uses the DFT to transform between spatial domain and wave number domain, we would like to include a simple example to illustrate the idea.

Consider a discrete time signal $u(m)$ consisting of N samples from $m = 0$ to $m = M_{max}$. Δm is the separation interval between samples. N has to be odd or we will need a small change in the formulae. Taking the DFT of $u(m)$ results in a N point signal in the Fourier domain ranging from $-K_{mmax}$ to K_{mmax} . In this example we use the normalized angular frequency from $-\pi$ to π instead of 0 to 2π as used in the previous section. Δk_m is the separation between the samples in the Fourier domain signal [19]. Such a Fourier transform pair is given in figure. 2.7.1.

In the following section, we will find the relationship between these various variables. As a signal with N samples contains $N - 1$ intervals:

$$M_{max} = \Delta m(N - 1) \quad (2.30)$$

$$2k_{mmax} = \Delta k_m(N - 1) \quad (2.31)$$

The sampling frequency of the signal will be $F_s = 1/\Delta m$, so according to the Nyquist sampling theorem,

$$2k_{mmax} = \frac{2\pi F_s}{2} = \frac{\pi}{\Delta m} \quad (2.32)$$

Consequently, we can write

$$\Delta k_m = \frac{2k_{mmax}}{N - 1} = \frac{2\pi}{\Delta m(N - 1)} = \frac{2\pi}{M_{max}} \quad (2.33)$$

And as a result,

$$M_{max} = \frac{2\pi}{\Delta k_m} = \frac{\pi(N - 1)}{k_{mmax}} \quad (2.34)$$

With the help of equations (2.33), (2.34) and figure 2.7.1, we have the relationships between all the variables for both DFT and IDFT.

The above equations can be used for Fourier transform from time domain to frequency domain and vice versa by changing m to t and k_m with ω and to transform Spatial domain signal in to wave number domain by changing m to x and k_m with k_x .

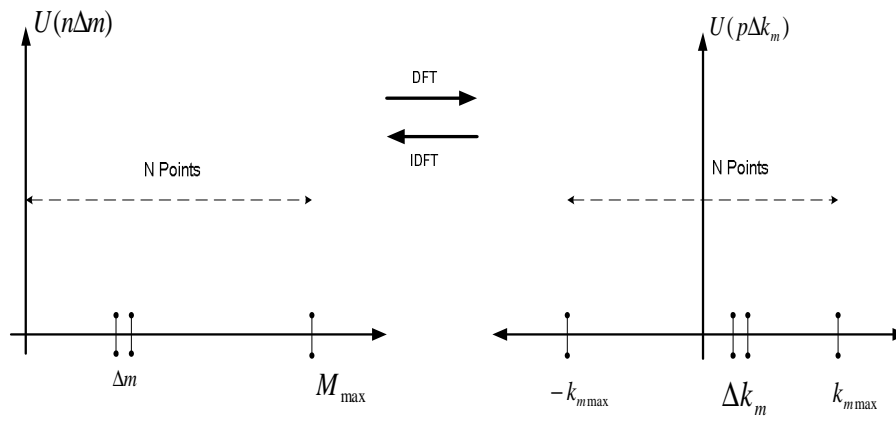


Figure 2.7.: Discrete Fourier Transform pair

Chapter 3:

3. Synthetic Aperture Radar Migration Algorithms

The term “Migration” refers to movement of recorded events to their true spatial positions [9]. This is done either by back-propagation or back-projection of the received signals. Environment is measured by the technique called Synthetic Aperture Radar (SAR) in which antennas perform measurement sweeps across the environment at pre-determined distances. The goal of the migration algorithm is then to use this data to refocus the reflections to their true positions and, if possible, extract their physical shape.

As seen in figure 2.3.1 (b), one point in the $S(X, Z)$ domain is shown as a hyperbola in B-scan $B(X, k)$. Now the task of migration algorithms is to refocus these hyperbolas back to the one point in $S(X, Z)$ i.e. to transform the data from time domain back into the depth domain, where depth corresponds to the distance of target from the antennas. Migration algorithms perform this in two different ways;

1. Refocusing using geometrical approaches without using wave theory. These methods do not take into account the phase of the received signal, instead use amplitudes of the delay bins to generate the image from the impulse response.
2. Using scalar wave equation and the received signal’s phase and amplitude. These methods have pretty complex math behind them but they provide more accurate focusing of the targets.

Furthermore, the data used by these methods can be either in frequency domain as transfer function shown in eq. (2.3), or in time domain as impulse response as seen in eq. (2.2).

Early on, these methods were mainly developed and used for Ground Penetrating Radar (GPR), airborne radar systems, seismology and tomography. Most of these methods are now finding themselves used and developed for UWB radar systems

and we are going to explain some of these migration methods in the following sections.

3.1. Back Projection and Back Propagation

As said before, SAR migration methods are divided into two categories, back projection and back propagation. Division of Migration algorithms into these two sub-divisions is given below:

- **Back-projection Algorithms:** Algorithms in this group use geometrical techniques to take the objects from time-domain to depth domain. These include the conventional SAR imaging called geometrical migration along with another simple migration called diffraction stack.
- **Back-propagation Algorithms:** These algorithm use wave theory to refocus the objects back to their true position. Algorithms in this group include Kirchhoff migration, F-K and phase-shift method.

3.1.1. Back Projection Algorithms

All imaging algorithms based on geometry do only spatial positioning and focusing of the targets without taking into account the phase of the received signal, instead they use amplitudes of the delay bins to generate the image from the impulse response. In the following section, such methods will be described in detail.

3.1.1.1. Diffraction Stack (TOA Estimation)

In this section, a geometrically based conventional SAR imaging method will be described. The basic model used in this migration algorithm is shown in Figure 2.3.1 (a) and also given below for easy access. The Time of Arrival (TOA) is the time a wave takes to travel from transmitter to the target and back to the receiver. Mathematically, TOA can be calculated by the eq. (3.1).

$$\text{TOA} = \frac{\sqrt{(x_{tr} - x_T)^2 + (z_{tr} - z_T)^2} + \sqrt{(x_T - x_{re})^2 + (z_T - z_{re})^2}}{c} \quad (3.1)$$

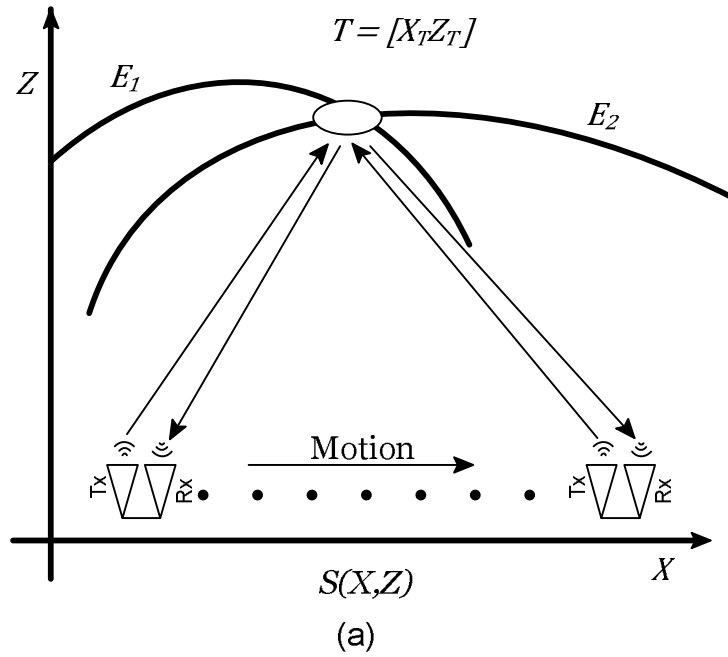


Figure 3.1.: a) Synthetic Aperture Radar

In eq. (3.1), transmitter is located at $[x_{tr}, z_{tr}]$, target is at $[x_T, z_T]$, and the receiver is located at $[x_{re}, z_{re}]$. c is the velocity of the wave inside the medium. The B-scan $B(X, k)$ shown in figure 2.3.1 (b) is showing a time domain representation of a point in space as a hyperbola. Now we can say that the received signal at a specific time can be reflected from any point corresponding to the locations having a constant TOA.

The algorithm coherently sums the received signals at each of the antenna positions onto the image map. I.e. for each antenna position the delay bin amplitudes corresponding to a specific distance are added to that particular pixel on the image map [10]. This is done for all the antenna positions.

This algorithm works as follows:

1. Divide complete area into a spatial grid with the desired resolution;
2. For each grid position, find the round trip time from transmitter to the target pixel and back to receiver;
3. Measure the impulse response of the channel for each antenna position.

4. Add the amplitudes of the received time bins to the pixels having the same TOA.

$$S(x_i, y_j) = \sum_{k=1}^N B(t_{ij}(k), k) \quad (3.2)$$

5. Perform steps 2, 3, and 4 for all the antenna positions.

Eq. (3.1) can be used for calculating the round trip time for each pixel of the spatial grid. In eq. (3.2), $S(x_i, y_j)$ contains the amplitudes of the pixels, $t_{ij}(k)$ is the TOA for each pixel (x_i, y_i) with N corresponding to the number of antenna positions.

3.1.1.2. Simple Wall Compensation

The method discussed in section 3.1.1.1, assumes that the medium between antennas and the target is homogeneous, but as in our case, there will be a wall in between them, we will have to compensate for the effects of the wall. A spatial model of through the wall propagation is shown in figure. 3.1.2.

For further calculations, let us assume a homogeneous and non-anisotropic wall with effective relative permittivity ϵ_{rw} present between the targets and the antennas. As the wave travels through the wall, its speed is reduced as compared to the air as the permittivity, permeability, and conductivity of the material of the wall is different from air. As a result, the TOA measured at the receiver will not correspond to the correct location of the target. The velocity of the wave inside the wall can be calculated by:

$$V_{wall} \approx \frac{1}{\sqrt{\mu_w \epsilon_w}} = \frac{1}{\sqrt{\mu_a \epsilon_a \mu_{rw} \epsilon_{rw}}} = \frac{c}{\sqrt{\mu_{rw} \epsilon_{rw}}}, \quad (3.3)$$

where ϵ_{rw} and μ_{rw} are relative permittivity and permeability of the wall respectively. For non-magnetic materials, $\mu_{rw} = 1$. Now the time to propagate through the wall is then given by:

$$t_{wall} = \frac{D_{wall}}{V_{wall}}, \quad (3.4)$$

where D_{wall} is the width of the wall. The time difference between free space and through the wall propagation is found by:

$$t_{difference} = \frac{D_{wall}}{c} (\sqrt{\epsilon_{r_{wall}}} - 1), \quad (3.5)$$

so the extra time taken by the wave to propagate through the wall twice can then be included into $t_{ij}(k)$ from eq. (3.2) as:

$$T_{ij}(k) = t_{ij}(k) + 2t_{difference} \quad (3.6)$$

The targets in compensated image are better focused and closer to their true positions behind the wall [10].

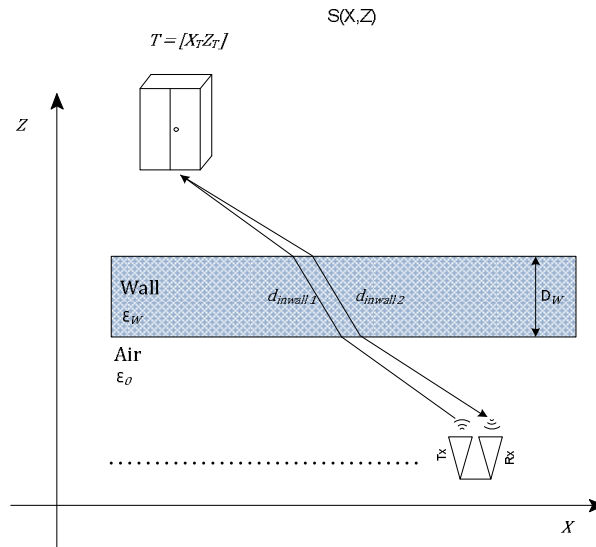


Figure 3.1.: Spatial model of wave penetrating through the wall

3.1.1.3. Differential SAR

Due to the presence of wall between the target and the antennas, there is always very strong wall reflection. In [11], authors have suggested the elimination of the direct reflection from the wall.

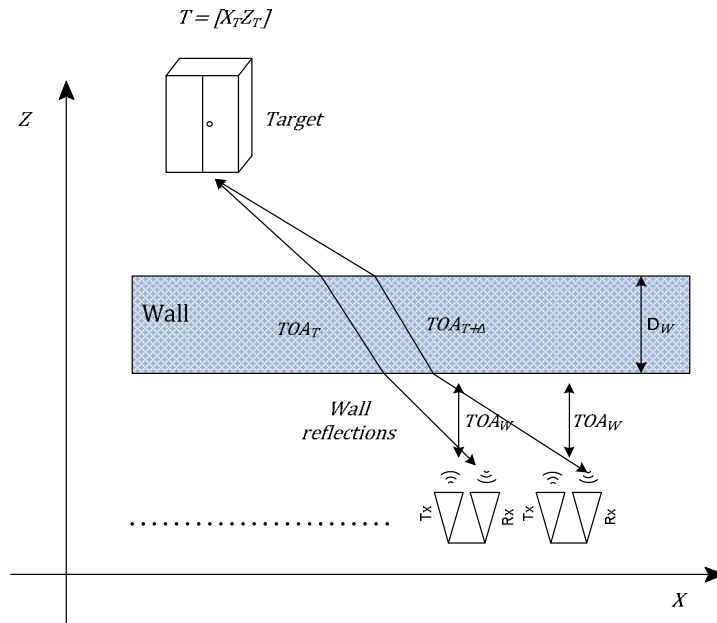


Figure 3.1.: Differential SAR model

During the SAR scanning, as seen in figure 3.1.3, all the objects seem to move due to the motion of antennas, but as the distance of the wall from the antennas is constant during the scan, the reflection from the wall remains almost constant for two consecutive antenna positions, whereas, the reflection from the objects behind the wall will not be the same.

Due to the elimination of the strong wall reflection, the signal to clutter ratio of small objects gets better for objects behind the wall. However, the wall has to be at the same distance from the antennas during two consecutive positions.

3.1.2. Back Propagation Algorithms

3.1.2.1. Exploding Reflector Model (ERM)

Migration algorithms contained in this category use the wave theory to migrate the reflecting objects from time domain back to the depth domain. These methods are based on the Exploding Reflector Model (ERM) which assumes that instead of EM waves starting from transmit antenna, getting reflected from the target and

received by the receive antenna, the wave field starts at the target reflector and propagating towards antennas with half the wave propagation speed.

The ERM says that the impulse response measured by the antennas along the cross-range is same to the response measured through a virtual array, the only difference between actual and virtual scans is that in actual scan the delay corresponds to the time it takes for a wave to travel to the target, get reflected, and come back to the receiver antenna, whereas, in virtual scan, the time delay only corresponds to the travel time between target and the receiver [15]. This is done by using one half of the propagation velocity in the calculations.

The Exploding Reflector Model is shown in figure. 3.1.4. Exploding Reflector Model can only be applied to the common offset radar configurations (transmit and receive antennas at the same position).

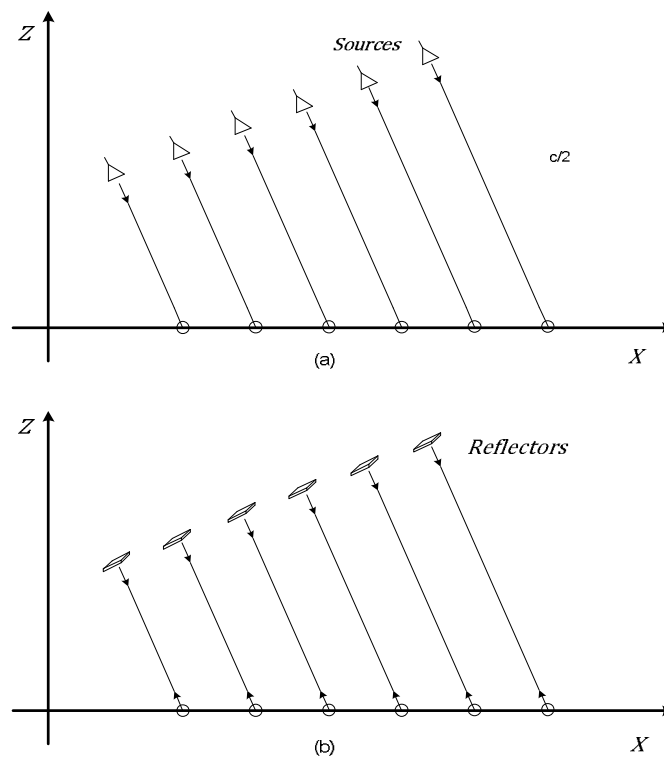


Figure 3.1.: a) ERM with wave field originating at target surface at $t = 0$ and propagating with half speed. b) Wave field leaving transmitter, gets reflected from the target surface and is received by the receiver.

In practical scenarios, the received waves at the antennas are not always coming directly from a reflector; instead the received waves can have higher order reflections resulting from reflections between closely placed target reflectors. This effect causes the rise of artifacts in the image generated by the migration algorithms and is investigated in scenario 2 given in section 6.2. The results in section 6.2 show the presence of an object behind the metallic plate, but in reality there is nothing there. These effects can be mitigated by use of directional antennas having small beamwidth.

3.1.2.2. Kirchhoff Migration

Kirchhoff migration is based on the solution of scalar wave equation. It is a fairly complicated algorithm and it is explained by the author in [12] in great detail. The Kirchhoff Migration algorithm is based on Exploding Reflector Model (ERM) and can be applied to the data acquired via Synthetic Aperture Radar (SAR) system using co-located transmit and receive antenna pairs (common offset case).

The objective of this migration technique is same as other techniques; i.e. to migrate the target objects from the time domain back to depth domain. Kirchhoff migration does this by back-propagating the scalar wave front received through SAR system to the object plane through the integral solution of the scalar wave equation.

Using the ERM's assumption that the wave field originates from the target's surface at time zero, propagating with half the propagation speed towards the receiver antenna; the migrated wave field $u(r', t)$ can be obtained from the following equation according to figure 3.1.5

$$u(r', t) = \frac{1}{2\pi} \iint \frac{\cos\theta}{vR} \frac{\partial}{\partial t} u\left(r, t + \frac{2R}{v}\right) dx dy \Big|_{t=0} \quad (3.7)$$

Where θ is the angle between cross range axis (x-axis) and the line joining the receiving antenna point r and the migration point r' . R is the distance between the point r and r' and v is the propagation velocity of the wave inside the medium.

Eq. (3.7) can only be used for the common offset cases and not in the cases where transmit and receive antennas are not in pair. Authors of [13] have proposed a modification in the integral formulation to make it compatible with the multi-static configuration as seen in figure 3.1.5.

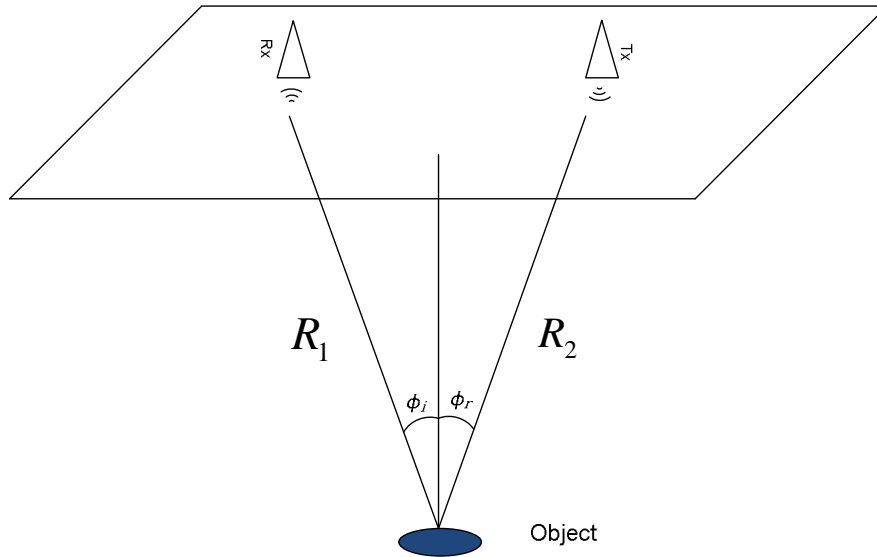


Figure 3.1.: A multi-static Antenna configuration.

The eq. (3.7) for multi-static configuration can then be written as

$$u(r', t) = \iint (\cos \theta_1 + \cos \theta_2) \frac{R_1 R_2}{v} \frac{\partial}{\partial t} u(r, t + \frac{R_1 + R_2}{v}) dx dy |_{t=0} \quad (3.8)$$

θ_1 and θ_2 can be seen as angle of arrival and angle of departure at the target r' in figure 3.1.5.

The range factor within the formulation ($R_1 R_2$) is used as an amplitude correction parameter, but its inclusion often amplifies the amplitudes of the side lobes. Due to this, the range factor is not included in the formulation resulting in

$$u(r', t) = \iint (\cos \theta_1 + \cos \theta_2) \frac{1}{v} \frac{\partial}{\partial t} u(r, t + \frac{R_1 + R_2}{v}) dx dy |_{t=0} \quad (3.9)$$

As a result of such linear formulation in eq. (3.9), the modified Kirchhoff Migration can be implemented quite fast for use in practical applications.

3.1.2.3. Phase-Shift Migration (F-K)

In 1978, Jenö Gazdag proposed the phase shift migration in [14]. Phase-Shift migration uses the scalar wave equation for migrating the data acquired through SAR techniques towards their true spatial positions. This technique is based on Exploding Reflector model (ERM) as explained in section 3.1.2.1.

According to the two-dimensional scalar wave equation given in eq. (2.23); an electro-magnetic field $u(x, z, t)$ is

$$\left[\frac{\partial^2}{\partial x^2} + \frac{\partial^2}{\partial z^2} - \frac{1}{c^2} \frac{\partial^2}{\partial t^2} \right] u(x, z, t) = 0 \quad (3.10)$$

Where x is the coordinate in the cross range (aperture) dimension, z in the range dimension, c is the wave propagation speed inside the medium. Taking the three-dimensional Fourier transform of the eq. (3.10) over x, z and t gives

$$\left(k_x^2 + k_z^2 - \frac{\omega^2}{c^2} \right) U(k_x, k_z, \omega) = 0 \quad (3.11)$$

Where k_x and k_z correspond wavenumber components in the x - and z - direction, respectively. As $U(k_x, k_z, \omega) \neq 0$, we must have

$$\left(k_x^2 + k_z^2 - \frac{\omega^2}{c^2} \right) = 0 \quad (3.12)$$

Giving us

$$k_x^2 + k_z^2 = \frac{\omega^2}{c^2} = k^2 \quad (3.13)$$

where k is the magnitude of the wavenumber vector. Eq. (3.13) is known as the dispersion relation for two-dimensional wave equation with constant velocity.

Taking two-dimensional Fourier transform of eq. (3.10) over x and t , and using the dispersion relation in eq. (3.13), results in a frequency-wavenumber (F-K) domain equation given as

$$\left[\frac{\partial^2}{\partial z^2} + (jk_z)^2 \right] U(k_x, z, \omega) = 0 \quad (3.14)$$

Here $-k_z^2$ is replaced by $(jk_z)^2$.

In case of ERM and radar applications, we only consider the waves travelling from the target to the receive antenna; i.e. negative z - direction. As a result, eq. (3.14) becomes

$$\frac{\partial}{\partial z} U(k_x, z, \omega) = -jk_z U(k_x, z, \omega) \quad (3.15)$$

The solution to the eq. (3.15) is of the form

$$U(k_x, z, \omega) = U(k_x, z = 0, \omega) e^{-jk_z z} \quad (3.16)$$

This equation shows that an extrapolation of the wavefield in the z -axis in the frequency-wavenumber (F-K) domain is a phase-shift operation. So, by recursively moving the wavefield along the z -axis with Δz steps, the wave-field can be reconstructed.

Assuming the frequency response of the channel measured using the stepped frequency radar system is given by

$$H(f, z = 0, x_p) = \sum_k a_k e^{-j2\pi f t_k} \quad (3.17)$$

Steps needed to generate the migrated image from the frequency response are as follows:

Step 1: In order to convert the frequency response into a wavefield, take Fourier transform of the frequency response from the spatial domain x into the wavenumber domain k_x

$$H^2(f, z_0 = 0, k_x) = \sum_{p=1}^P H(f, z_0 = 0, x_p) e^{-jk_x x_p} \quad (3.18)$$

The DFT in this step can be implemented by using FFT for computational efficiency.

Step 2: Propagate the wavefield to $z_1 = z_0 + \Delta z$ by appropriate phase-shift in z -axis.

$$H^2(f, z = z_1, k_x) = H^2(f, z_0 = 0, k_x) e^{-jk_z \Delta z} \quad (3.19)$$

Where k_z denotes the wavenumber along z direction and is given by the wave dispersion equation as

$$k_z(f, k_x) = \sqrt{\left(\frac{2\pi f}{c}\right)^2 - k_x^2} \quad (3.20)$$

c in eq. (3.20) is taken as half the propagation speed of the wave inside the medium.

Step 3: Taking inverse Fourier transform of the wavefield over k_x and f domain in two steps, we get the temporal response of the system as

$$H(f, z = z_1, x) = \Delta x \sum_{k_x} H^2(f, z = z_1, k_x) e^{jk_x x} \quad (3.21)$$

Then

$$h(t, z = z_1, x) = \frac{\Delta f}{B} \sum_f H(f, z = z_1, x) e^{j2\pi f t} \quad (3.22)$$

Step 4: Repeat steps 2 and 3 for the total range i.e. $z_{m+1} = z_m + \Delta z$ with $m = 0, 1, \dots, M - 1$.

The resulting migrated image is created by examining the temporal response given in eq. (3.22) at $t = 0$.

In order to compensate for the varying wave velocity during the wave propagation (via different propagation medium), c in eq. (3.20) has to be a function of z ; i.e. $c(z_m)$, containing velocity of the wave for each Δz interval, assuming the velocity of wave to be constant inside a Δz interval.

Chapter 4:

4. Selection of Algorithms and Analysis

Up till now, we have discussed various migration techniques for Ultra-Wideband radar and we divided them into two major categories; back-projection and back-propagation. Both of these categories contain migration techniques which take completely different approaches to get the image from the measured data which can be either in frequency domain (Transfer Function) or in time domain (Impulse Response). Back-projection techniques use geometrical approach and back-propagation techniques use wave theory to get the migrated image.

Comparison of different migration techniques, being an important part of this master's thesis project, had to be done. So, we selected two migration algorithms from the two main categories of migration techniques, named Diffraction Stack (Geometrical Migration) and Phase-Shift (F - K) Method.

The selection of Diffraction Stack is obvious as it is the main technique belonging to the back-projection group. On the contrary, the selection of a method to be implemented from the back-propagation group was not simple, but we selected Phase-Shift method due to its faster implementation, computational efficiency, better focusing of the target objects and the ability to compensate for the varying velocity inside the medium [15].

4.1. Synthetic Data Generation

Implementation of algorithms was verified using synthetic data generated in the frequency domain using the operational frequency band of the system. Assuming co-located isotropic transmit and receive antennas and point scatterers, we sum the backscatter coming from each defined point scatterer arriving at the aperture without including the interactions between them; i.e. for each antenna position and frequency, we sum up all the complex exponentials corresponding to the defined point scatterers according to the following equation;

$$H(f, x_p) = \sum_f I_{ref} e^{-\frac{j2\pi f}{c} 2D} \quad (4.1)$$

Where I_{ref} is the reflection coefficient of the point scatterer, c is the propagation speed and D corresponds to the distance between the point scatterer and the receiving antenna x_p .

The $H(f, x_p)$ is the transfer function which can be used directly in the Phase-Shift algorithm but it needs to be converted into impulse response $h(t, x_p)$ as Diffraction Stack algorithm uses data in this form. This can be accomplished by computing the inverse fast Fourier transform (IFFT) of the transfer function.

As an example, assume a 2 meter linear array in the frequency band of 9 to 16.5 GHz with co-located transmit and receive antennas placed with 1 cm of separation in the array. A point scatterer placed 1 meter away from the center of the aperture i.e. at $S(x, z)$ with $x = z = 1$ m. Synthetic Data is generated with a frequency step $\Delta f = 5$ MHz. The impulse response of the example scenario for all the antenna positions is generated by taking the IFFT of the synthetic data from frequency into the time domain. The scenario is given in figure 4.1.1, and the top view of the impulse response for all the antenna positions (B-scan) is given in figure 4.1.2.

$$S(X,Z) = 2 \times 2 \text{ meters}$$

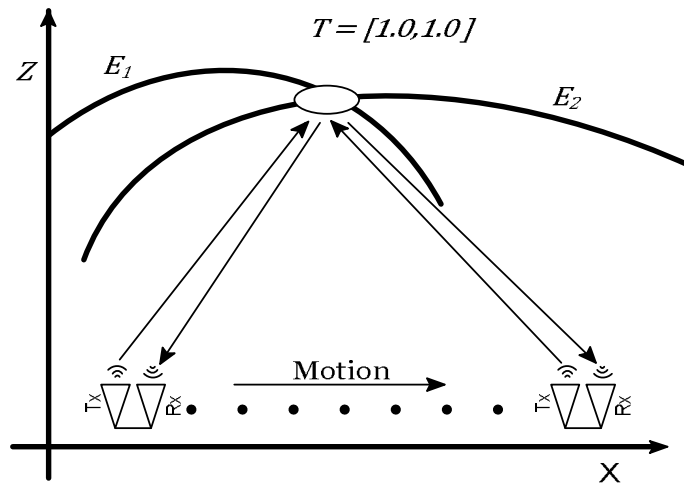


Figure 4.1.: Point Scatterer located at 1 meter away from center of the antenna aperture

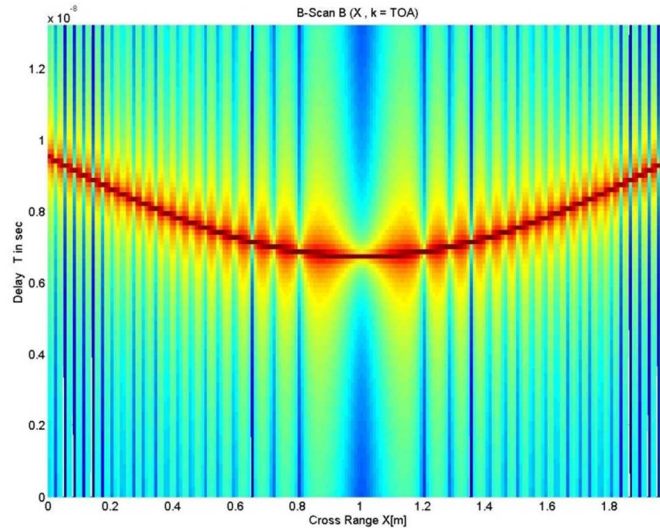


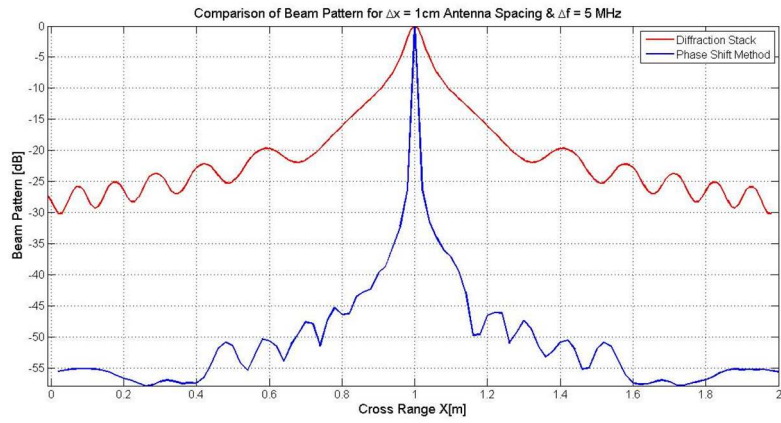
Figure 4.1.: B-scan $B(X, k = TOA)$.

4.2. Comparison of Migration Methods

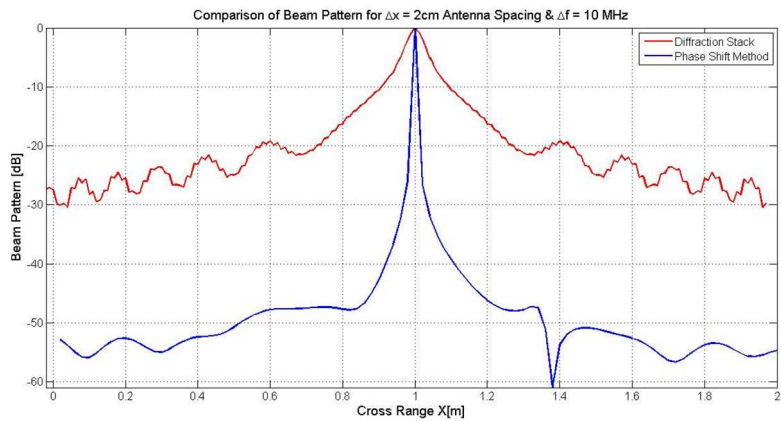
In this section, we will apply both algorithms to the synthetic data generated according to the method described in the section 4.1. The metric of comparison is taken as the side lobe level achieved by the algorithms.

4.2.1. Performance for Point like target

For this simulation, we will use a 2 meter linear array operating in the frequency range of 9 to 16.5 GHz with a total of 7.5 GHz bandwidth. The selection of this frequency range is discussed in section 5.3.1. The antenna separation in the linear array is $\Delta x = 1$ cm and 2 cm with the frequency increments of $\Delta f = 5$ MHz and 10 MHz. A point scatterer is placed at 1 meter from the center of the linear array and co-located antennas assumed. Algorithms are applied onto the data to get 2-D migrated images which are then integrated over a small range to get a 1-D image showing the spatially distributed grating lobes. The resulting beam patterns are shown in figure 4.2.1.



(a)



(b)

Figure 4.2.: Theoretical beam pattern obtained by diffraction stack and Phase Shift method for a) $\Delta f = 5$ MHz and $\Delta x = 1$ cm, and b) $\Delta f = 10$ MHz and $\Delta x = 2$ cm

As seen in the figure 4.2.1, the Phase-Shift method is giving much narrower beam width as compared to the Diffraction Stack method, and the level of side lobes is also very low for Phase-Shift method. Moreover, the increase in antenna separation Δx and frequency step Δf does bring a bit of jitter in the side lobes of the beam pattern for both Diffraction Stack and Phase-Shift method.

The computational time taken by Phase-shift method is much shorter than Diffraction Stack due to the use of Fast Fourier Transform to generate the migrated images. Whereas the implementation of Diffraction Stack algorithm

contains 3 nested loops thus requiring longer computational time for generating the image.

4.2.2. Performance for Closely-Placed targets

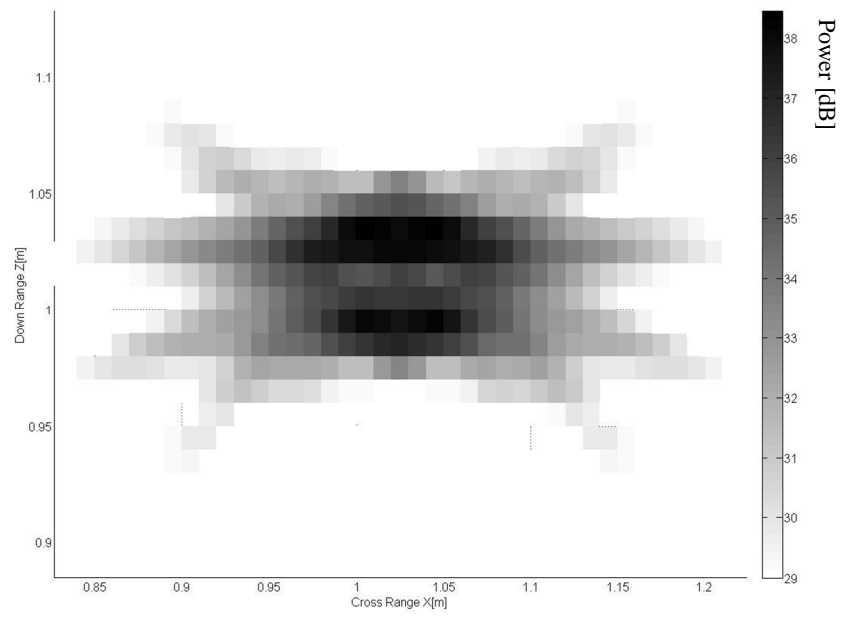
Assuming four point scatterers placed 4 cm apart from each other in a rectangular fashion are used to generate the synthetic data. Bandwidth taken is 7.5 GHz, $\Delta x = 1$ cm of antenna spacing and $\Delta f = 5$ MHz of frequency separation. The resulting images generated using both algorithms are shown in figure 4.2.2 with the scale showing power levels in dB.

These resulting images show the overall performance of both the algorithms. It is clearly seen that Phase-Shift algorithm provide much more sharper image as compared to Diffraction Stack algorithm when the threshold (Max – Min power level) for the side lobe level is set at -10 dB. The selection of threshold level is very important for making the resulting image clearer as the side-lobe levels generated by Diffraction Stack are much higher than images generated by Phase-Shift method. Also, if the threshold level is selected very low then the smaller reflections will not be visible in the resulting image.

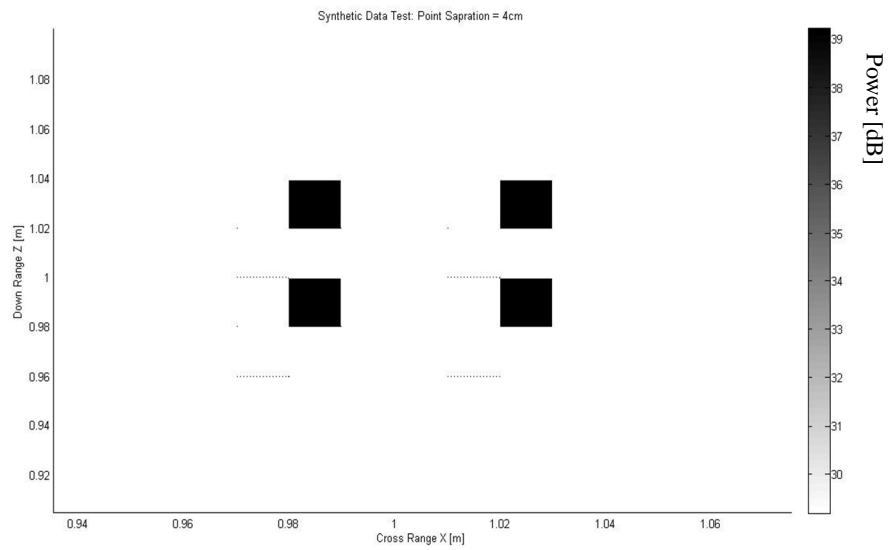
It is seen clearly in the figures 4.2.2 a) and b) that the Diffraction Stack algorithm generates much higher side lobes closer to the scatterers, whereas, Phase-Shift method refocuses the energy within a much smaller area close to the target scatterers.

Another interesting thing to see is that the scatterers along z-axis can be independently seen in the image resulted from Diffraction Stack algorithm figure 4.2.2 (a), whereas, scatterers along x-axis can be seen separately in the image resulted from Phase-Shift method figure 4.2.2 (b).

All of the above simulations were done without including noise in the transfer function. Based on the results using synthetic data, it is seen that the performance of DS algorithm is poorer as compared to PS algorithm and that PS algorithm is capable of distinguishing closely placed objects up to a distance of 4 cm, whereas, high side-lobe levels generated by the DS algorithm cause the objects with a separation less than 5 cm to be inside the side-lobes of each other.



(a)



(b)

Figure 4.2.: Numerical simulation of distributed targets. a) image obtained by Diffraction Stack algorithm, b) image obtained by Phase-Shift Method.

Now as we have established that the Phase-Shift method provides good results for closely placed targets, another example for the closely placed point targets is given below; with the scenario layout given in figure 4.2.3, Impulse Response (FFT of synthetically generated transfer function) given in figure 4.2.4, and the resulting image from the Phase-Shift migration are shown in figure 4.2.5.



Figure 4.2.: Closely placed point targets

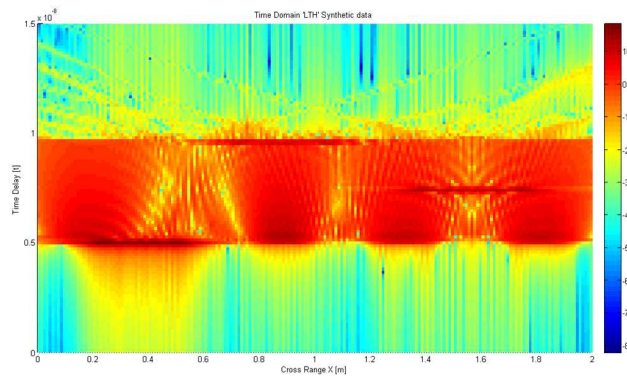


Figure 4.2.: Synthetic Impulse Response

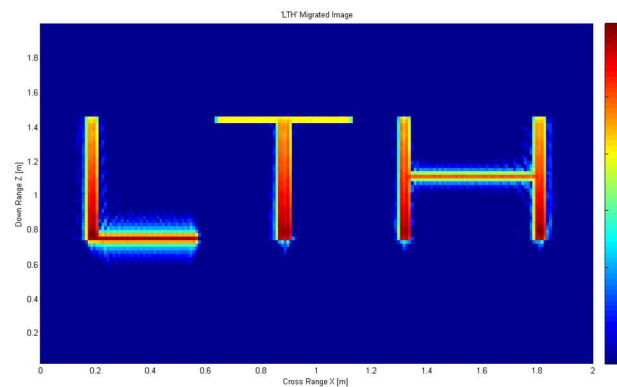


Figure 4.2.: Migrated Image by Phase-Shift Migration

Chapter 5:

5. UWB Radar Devices and Setup

In this chapter, we will be explaining the devices used for our UWB radar setup. Figure 5.1.1 contains a detailed block diagram of our radar system. UWB radar system consists of a Vector Network Analyzer (VNA), a laptop computer controlling the VNA, two 10 meter long coaxial cables, two Vivaldi antennas, a Low Noise Amplifier (LNA), a 9 meter long rail, a DC motor, and a trolley for moving the antennas over the rail.

5.1. UWB Radar System Design

5.1.1. Vector Network Analyzer (VNA)

A Vector Network Analyzer (VNA) is used to measure the frequency response of a channel which could be either a wireless channel with a transmit antenna connected to *port 1* of the VNA and a receive antenna connected to *port 2* of the VNA, or a wired channel where a cable is used to connect the two ports of the VNA. As we are going to use the stepped frequency continuous wave radar system (SFCW), this device is going to be the most important part of the complete system.

The VNA operates by exciting the TX antenna, which radiates the channel with discrete tones f from a wide frequency band from *port 1* and then measuring the signals received by the RX antenna connected to *port 2*. The parameter S_{21} contains the relative amplitude and phase information of *port 2* with respect to *port 1*. The operating frequency range (bandwidth B) of the system and the frequency steps Δf are selected by the user.

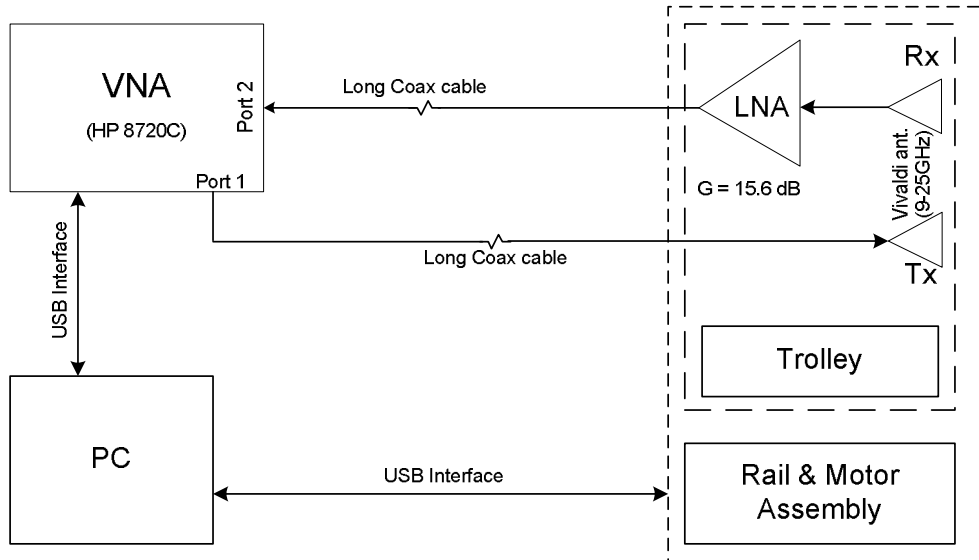


Figure 5.1.: Block Diagram of UWB Radar System

As an example, assume an UWB application with a frequency band of 3 to 8 GHz (6 GHz bandwidth) with a frequency step Δf of 3.75 MHz, resulting into 1601 frequency points, it will be able to detect a maximum multipath spread of:

$$T = \frac{1}{3.75 \times 10^6} = 266 \text{ ns}, \quad (5.1)$$

which corresponds to a total distance of 80 meters which is enough for small testing environments. As seen from the above discussion, if the number of frequency points are reduced, the Δf will increase resulting a small T , so the selection of these parameters should be done with care.

Now as the environment is going to be measured from different antenna locations (SAR technique), the measurement data had to be saved for every position. In order to automate this, we used an application developed in Labview® (a National Instruments software) to control the VNA functions and a DC motor to move the antennas over the rail. The computer is connected to the VNA via a USB port. The S_{21} data collected by the VNA for each antenna position is saved by the Labview program which is then ported into Matlab® for analysis.

The VNA used in our setup is HP 8720C and has an operating range of 50 MHz to 20 GHz. The dynamic range of VNA for IF bandwidth of 10 Hz is given in the table 5.1. This table is taken from the original product specification manual [20].

	Frequency Range in GHz			
	0.05 – 0.5	0.5 – 2	2 – 8	8 - 20
Maximum Receiver Power (<0.1 dB compression)	+20 dBm	+13 dBm	+10 dBm	+10 dBm
Maximum Source Power (at test ports)	+10 dBm	+10 dBm	+10 dBm	+10 dBm
Receiver Noise Floor (sensitivity)	-65 dBm	-90 dBm	-93 dBm	-93 dBm
Receiver Dynamic Range	85 dB	103 dB	103 dB	103 dB
System Dynamic Range	75 dB	100 dB	103 dB	103 dB

Table 5.1: Dynamic Range of HP 8720C VNA for IF bandwidth = 10 Hz [20]

The frequency range used in our radar setup is 9 – 16.5 GHz, having 1601 discrete frequencies with an IF bandwidth of 1 KHz. So, according to table 5.1, the system dynamic range and the receiver noise floor (receiver sensitivity) of our radar system, with 1 KHz IF bandwidth is;

$$\begin{aligned}
 \text{System Dynamic Range}_{10\text{ Hz}} &= 103\text{dB} \\
 \text{System Dynamic Range}_{1\text{ KHz}} &= 103 - 20 = 83\text{dB} \\
 \text{Receiver Sensitivity}_{10\text{ Hz}} &= -93\text{dBm} \\
 \text{Receiver Sensitivity}_{1\text{ KHz}} &= -93 + 20 = -73\text{dBm}
 \end{aligned} \tag{5.2}$$

The receiver sensitivity (noise floor) for IF bandwidth of 10 Hz is -93 dBm, as given in table 5.1, so for IF bandwidth of 1000 Hz, the noise floor of the system increases by 100 times which corresponds to 20 dB, which results in receiver sensitivity of -73 dBm. Similarly, the system dynamic range is reduced to 83 dB due to 1000 Hz IF bandwidth.

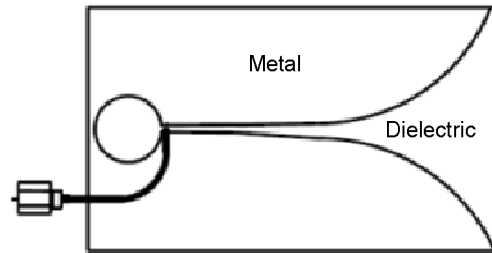


Figure 5.1.: Vivaldi Antenna with a coaxial connector

5.1.2. Antenna Selection

The antennas selected for use in the radar system are Vivaldi antennas operating in the frequency range of 9 to 25 GHz. The Vivaldi antenna is shown in figure 5.1.2. Vivaldi antennas are directional and wideband antennas which are suitable for use in the radar system considered here. Directional antennas are preferred in radar systems as they irradiate reflectors only in target direction, and reduce the reflections from walls and objects in other directions especially from the reflectors (wall) directly behind the antennas. Another reason of their selection was their small size and weight as the rail on which the antennas are supposed to move does not support heavy antennas like horn and log-periodic antennas.

The Vivaldi antennas used in our measurements have a typical gain of 8 to 10 dBi with the main lobe in front of the antennas. Both the antennas are mounted on a small trolley which is placed on a 9 meter long rail. A picture of the trolley is shown in figure 5.1.3. As seen in figure 5.1.3, transmit antenna is placed above the receive antenna with a separation of 11.5 cm. The distance of transmit antenna from the ground is approximately 140 cm.

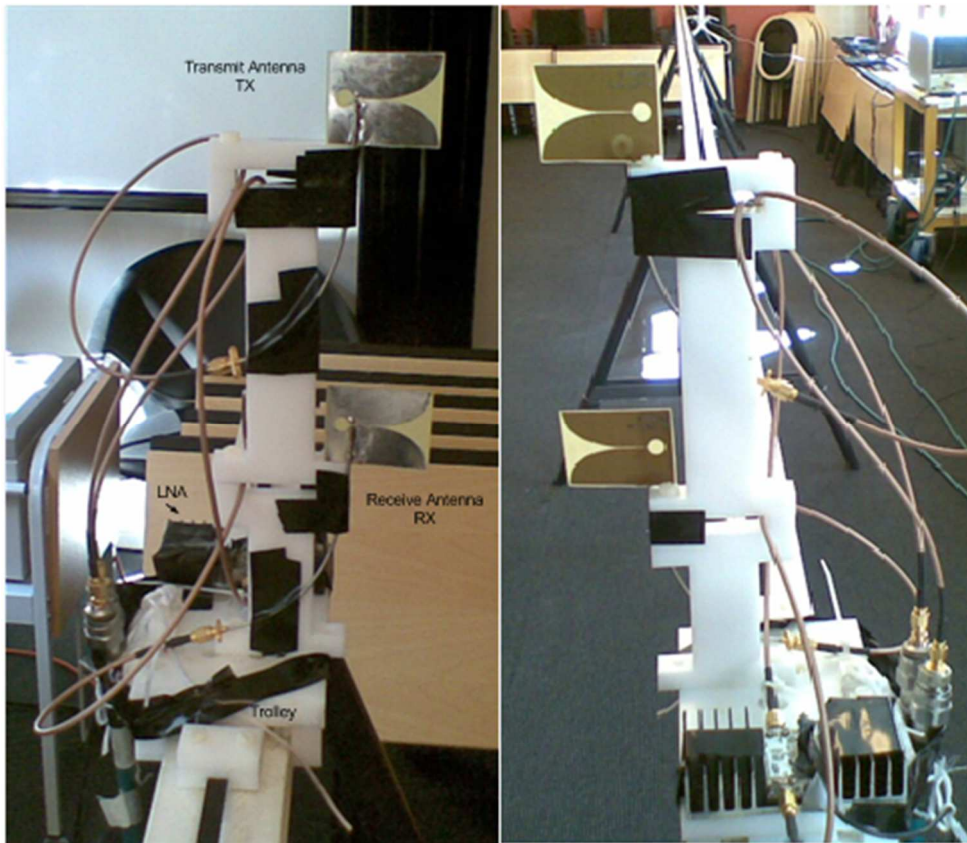


Figure 5.1.: Trolley with Tx and Rx antennas

5.1.3. Devices Connection Setup

The complete device connections are shown in figure 5.1.1, where *port 1* of the Vector Network Analyzer (VNA) is connected to the transmit antenna via a 10 meter long coaxial cable. The Receive antenna is connected to the input port of an LNA having a gain of about 15.6 dB in the frequency band of 9 – 16.5 GHz. The output port of the LNA is connected to *port 2* of the VNA via another 10 meter long coaxial cable. Both antennas and LNA are mounted on a trolley as shown in figure 5.1.3. This trolley is placed on a 9 meter long rail and is connected to a DC motor via a non-stretching rubber belt. The DC motor is capable of moving the trolley with 1 cm granularity and is controlled by the Labview® application developed at the department of electrical and information technology, EIT-LTH, through the USB interface.

The resulting complete radar system overview is given in figure 5.1.4.

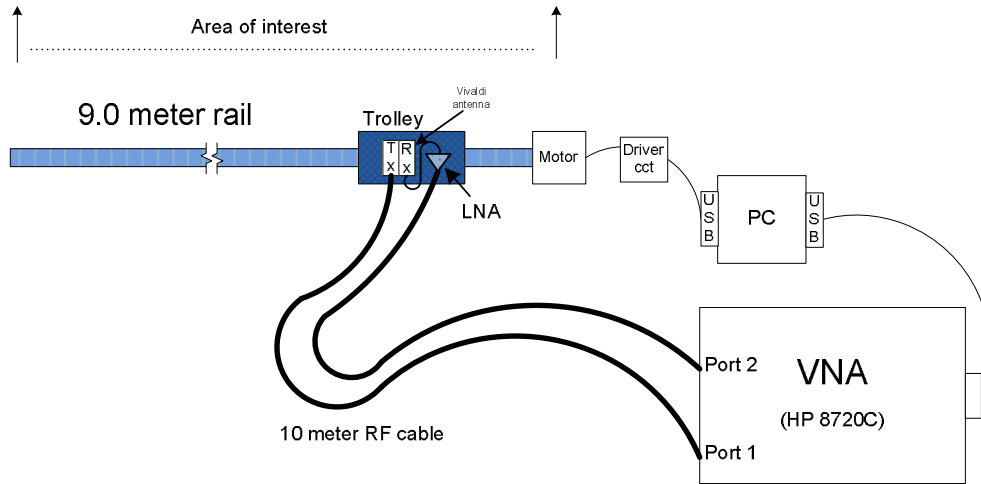


Figure 5.1.: UWB Radar System Overview

5.2. Channel Measurements

Considering figure 5.1.4, we are mainly interested in the relative amplitude and phase of *port 1* and *port 2* called S_{21} . During the frequency scan, VNA emits a frequency tone f from *port 1* and then measures the relative amplitude and phase $S_{21}(f)$ with respect to *port 2* as given in eq 5.2, where $X(f)$ is the signal at *port 1* and $Y(f)$ is the signal at *port 2*. This method automatically results in phase synchronization between the two ports. The signal leaves the transmit Vivaldi antenna, gets reflected and scattered from the surrounding objects and is received by the receive Vivaldi antenna. The signal is amplified by the LNA connected between receive antenna and coaxial cable connecting to the port 2 of VNA. Due to the absence of any absorber between transmit and receive antennas, there is a strong direct component present. The reflections from the ground directly below the receive antenna is very low as the main lobe of the antenna has very low gain in that direction.

$$S_{21}(f) = \frac{Y(f)}{X(f)} \quad (5.3)$$

The measured S_{21} parameter for each antenna position according to the figure 5.1.1 contains the transfer function as a product of the cable, Tx antenna, propagation channel, Rx antenna, and the LNA and can be written as:

$$S_{21}(f)_{meas} = H_{cab}(f) \cdot H_{Tx}(f) \cdot H(f, z = 0, x_p) \cdot H_{Rx}(f) \cdot H_{LNA}(f) \quad (5.4)$$

$H_{cab}(f)$ and $H_{LNA}(f)$ are measured after the measurements and then removed from $S_{21}(f)_{meas}$, leaving only the product of $H_{Tx}(f) \cdot H(f, z = 0, x_p) \cdot H_{Rx}(f)$ in the $S_{21}(f)_{corrected}$ i.e. $S_{21}(f)_{corrected}$ contains only the effects of Tx antenna, propagation channel, and the Rx antenna.

5.3. System Parameters

As said before, in order to get a good cross-range resolution, we need an aperture length of several meters. This is accomplished by using a 9 meter long rail to get synthetic aperture length of 8.5 meters for our radar system. The frequency range used in our radar system is from 9 to 16.5 GHz yielding 7.5 GHz of frequency bandwidth. The frequency step Δf used is approximately 4.68 MHz by using 1601 frequency points over a bandwidth of 7.5 GHz.

5.3.1. Selected Bandwidth

The best frequency range for through the wall radar imaging systems is 3 – 5 GHz as signals in this frequency range can pass through walls without much attenuation [2], due to which, the bandwidth of 2 – 8 GHz has been majorly used for through-the-wall radar imaging systems. As the frequencies higher than 8 GHz have not been used for the similar radar systems, we decided that it will be interesting to investigate the frequency range of 9 – 16.5 GHz in our radar system. The selection of such high frequency range has its own pros and cons which are;

- Free space path loss $\left(\frac{4\pi d}{\lambda}\right)^2$ and cable (20 meters) attenuation increases with the increase in frequency, resulting in higher power losses in the band of interest resulting in a lower received power level.
- Higher frequencies suffer from higher attenuation when passing through materials which further reduces the received power levels.
- One advantage of selection of such higher frequency range is the fine cross-range resolution δx achievable by the radar system.

So, the selection of this high frequency range results in lower received power due to free space losses, cable attenuation, and attenuation in the wall materials, but it does result in a much finer δx .

5.3.2. Frequency Step Interval Δf

Use of discrete frequency spectrum $Y(f)$ causes the received *sinc* pulses to be periodic with interval $T = 1/\Delta f$ [15]. The selection of $\Delta f = 4.68$ MHz allows us to detect multipath arrivals in time for up to $T = 213$ nsec, which is sufficient in our selected scenario as the maximum distance we want to see is 20 meters (to the target and back) corresponding to $T = 66$ nsec, upon including the cable lengths (20 meters with wave propagation speed of $2/3 c$), the required T becomes 176 nsec.

5.3.3. Cross Range Sample Interval Δx

The Vivaldi antenna, being directive, only detects an object when it lies within its beamwidth. The chord length of the antenna is close to zero at the antenna position which increases when moving further away from the antenna. The beamwidth of our Vivaldi antennas is not known, additionally, it also changes with the increase in frequency. Assuming a beamwidth of the antenna to be 35° , the chord length at a distance 50 cm away from the antenna is 30 cm.

$$Z = 0.5 \times 2 \times \sin\left(\frac{35}{2}\right) = 0.30 \quad (5.5)$$

So in order to cover all the area in front of the antenna aperture, we need to set $\Delta x \leq 30$ cm. In order to increase the total received power from each scan position [15], $\Delta x = 2$ cm was chosen resulting in a total of 425 antenna positions for an aperture length of 8.5 m. The number of sampling intervals affects amount of information extracted from the environment, the resolution of the migrated image, and the power levels of the target peaks with higher peak levels for smaller sampling intervals with respect to larger intervals.

5.3.4. Down-Range Resolution δz

The ability to differentiate between signals arriving from both the target and the immediate surroundings is very important in terms of range resolution, δz , of the radar system. This is possible when the time difference between both arrivals is greater than the pulse width δt . As the channel is measured in frequency domain, the spectrum $X(f)$ in frequency domain translates into *sinc* pulses with width $\delta t = 1/B$ in time domain. Using the pulse width δt in eq. (2.1), the range resolution becomes;

$$\delta z = \frac{c \times \delta t}{2} = \frac{c}{2 \times B} = 0.02\text{m} \quad (5.6)$$

the range resolution, δz , of the system, for bandwidth of 7.5 GHz, is thus 2 cm.

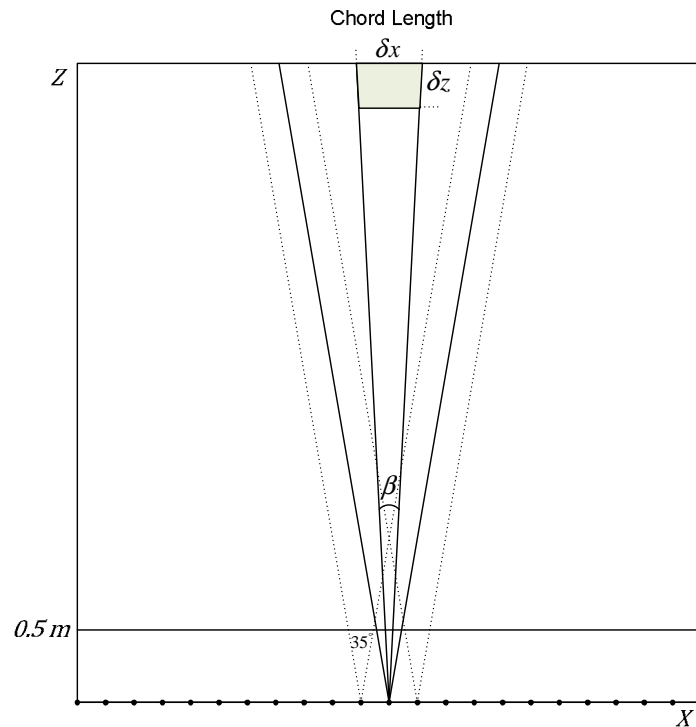


Figure 5.3.: Range and Cross-Range Resolution

5.3.5. Cross-range Resolution δx

One of the main advantages of the synthetic aperture radar is its ability to provide a fine cross-range resolution δx by reducing the real beam width of the antenna. According to the authors of [15], the synthetic beam width of a SAR system is $\beta = \frac{c}{2f_c X}$ as seen in figure 5.3.1. Here $f_c = 12.75$ GHz and the X is the synthetic aperture size 8.5 m which results in $\beta = 1.4 \times 10^{-3}$. For such small angles, the chord length δx is approximately equal to the $\beta \cdot Z$ where Z is the maximum range of the radar system,

$$\delta x = \frac{c \cdot Z}{2 \cdot f_c \cdot X} \quad (5.7)$$

Eq. (5.7) shows that the cross-range resolution δx of our radar system strictly depends upon the maximum range of the radar. By taking $X = Z$, the cross-range will only depend upon the center frequency f_c which is 12.75 GHz. So for our radar system, δx is approximately 1.2 cm which is of the order of range resolution δz which is 2 cm.

The theoretical achieved image resolution is shown in figure 5.3.2.

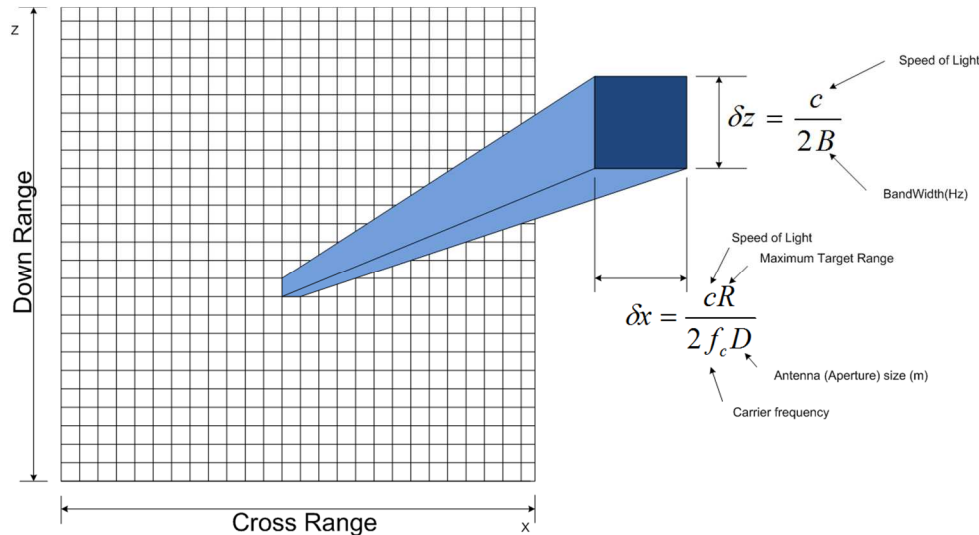


Figure 5.3.: 2D Image Resolution

5.3.6. Radar System Limits

Our radar system is mostly limited by the selection of system bandwidth and the frequency range. The range and cross range are all connected with the bandwidth. Simply saying, higher the bandwidth, greater will be the image resolution and the ability to recognize the target's shape. The antenna aperture length and antenna beam width are also important in order to see all the targets in front of the antennas. The radar system being a forward looking system, the antenna aperture needs to be in front of the area of interest. Also, the radar system can only work with directional antennas in order to avoid reflections from the back of the antennas, however, omni-directional antennas could be used with absorbers at the back in order to get rid of reflections from the rear of the antennas.

The achieved resolution and the resolution error for scenario 1 for an antenna sampling interval of 2 cm and using full bandwidth is given in the table 5.2;

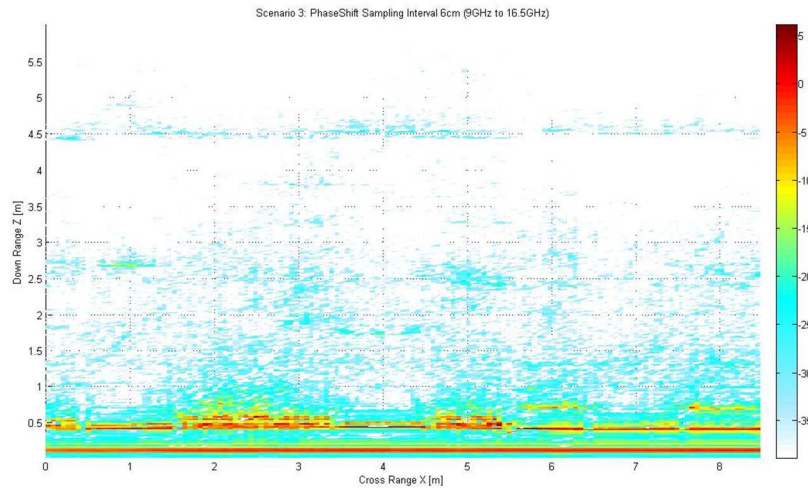
Migration Algorithm	Down-Range		Cross-Range	
	Resolution	Error	Resolution	Error
Phase-Shift	2 cm	± 2 cm	2 cm	± 1 cm
Diffraction Stack	2 cm	± 2 cm	5 cm	± 2.5 cm

Table 5.2: Practical Resolution of the Algorithms

The detail of these figures is given later in section 6.4.

The strong direct component between the antennas is seen with highest power in the generated radar image which remains constant for each antenna position. The reflections from the targets are much lower than this component, which is compensated by taking multiple samples along the synthetic aperture, resulting in higher peaks at the target location in the generated radar image.

In practical scenarios, the cross-range resolution is also dependent on the antenna sampling interval with higher intervals leading to poor resolution and less information about the environment. The effects of having a larger sampling interval are shown in figure 6.3.3. Due to higher sampling interval $\Delta x = 6\text{cm}$, among other things, the studs inside the wall are not visible in a), whereas, they are clearly visible in b) for $\Delta x = 2\text{cm}$.



a)

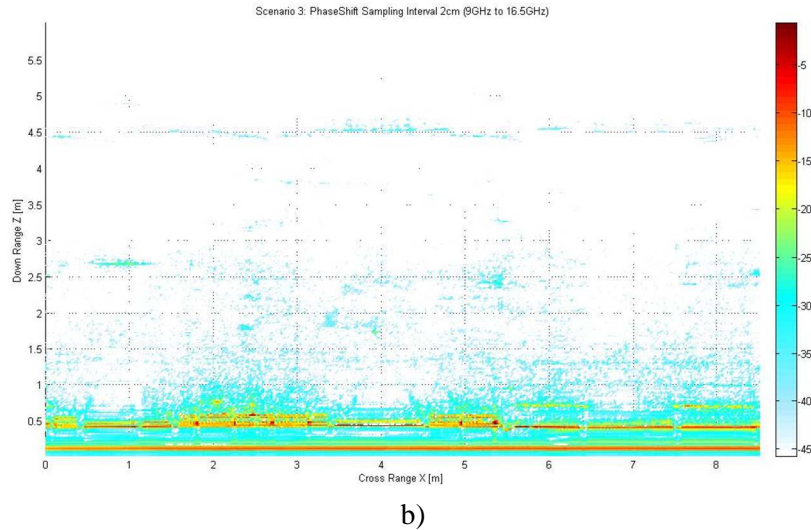


Figure 5.3.: PS results for scenario 3 with a) $\Delta x = 6cm$, and b) $\Delta x = 2cm$

One major limitation on the radar system when using the Diffraction stack algorithm is the ability to discriminate between two strong reflectors placed close to each other, let us say, 10 cm due to the high side lobe levels. On the other hand, due to very low side lobe levels, Phase-Shift method can discriminate between closely placed reflectors with much better accuracy.

The objects with good reflectivity can be located easily by our radar system but objects with lower reflectivity are not shown clearly in the migrated image which is obvious. Also the distance from the antenna is important as the power of the reflection received from distant targets is small which leads to lower signature in the migrated image.

5.4. Signal Processing Steps

To convert the SAR measurement data into a state where it can be used by the migration algorithms requires several signal processing steps. The requirement on the data S_{21} is that it should only contain the effects of the channel and antennas, but the original data received after the measurements contains the effects of two 10 meter long cables connecting antennas to the two ports of the VNA according to eq. (5.4). It also contains the effects of the amplifier and the small wires which

are soldered onto the Vivaldi antennas. So the data correction was an essential step to make this measurement data in a useful state.

5.4.1. Received Transfer Function

The received S_{21} for a single antenna position is shown in figure 5.4.1. It is seen that the received power level starts decreasing after 12 GHz with the peak level being at 10.8 GHz. Power level becomes stable upon reaching 13.8 GHz and stays within 5 dB up till 16.5 GHz. During this decline, the received power drops from -45.2 dB to -75 dB, a loss of 30 dB. This is due to the following reasons;

- The free space path loss, which increases with the increasing frequency.
- Cable losses, as the attenuation increases with increasing frequency.
- The antenna gain over the entire frequency range may not be same.
- The directivity of the antennas increase with increasing frequency, resulting in the power of direct component getting lower, giving less overall received power.

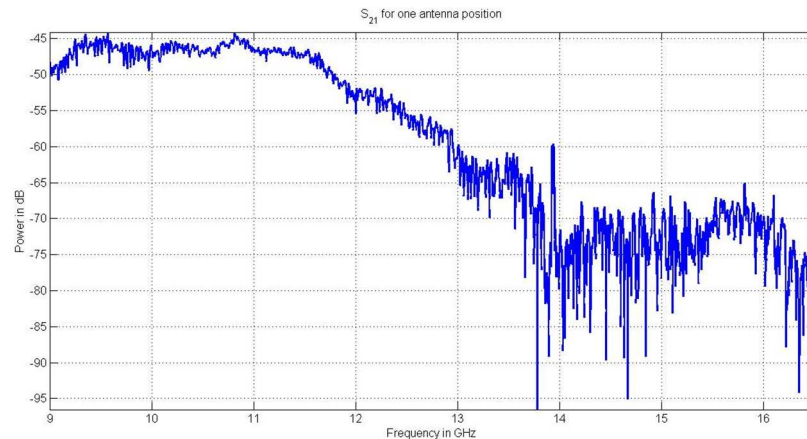
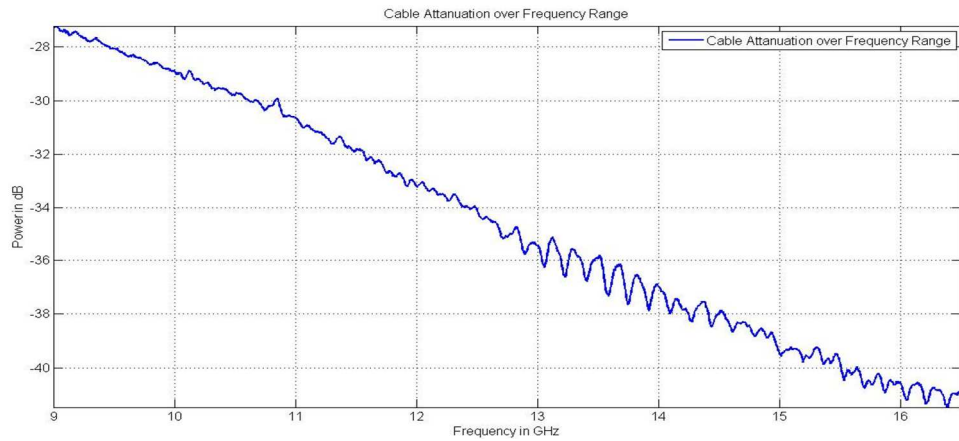


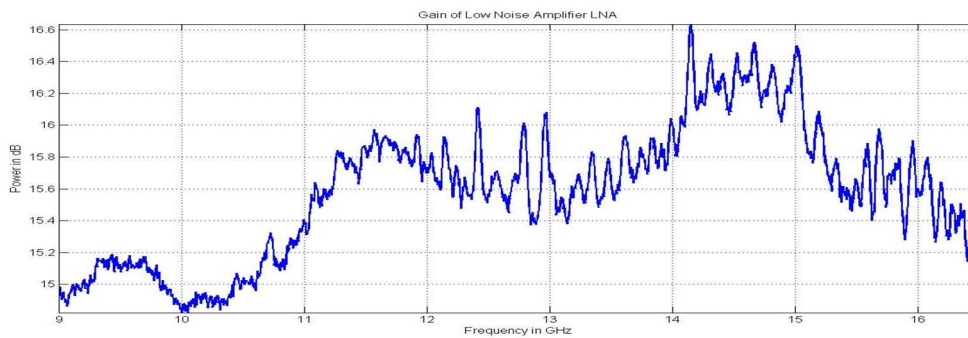
Figure 5.4.: S_{21} for a single antenna position

5.4.2. Effects of Cables and LNA

After the measurements, the effects of cables and LNA were measured so that they could be removed from the S_{21} leaving only the effects of antennas and environment. As said in section 5.4.1, the attenuation caused by the 20 meter long cables depend upon the frequency. This phenomenon is clearly seen in figure 5.4.2 a) with the response of LNA given in figure 5.4.2 b).



a)



b)

Figure 5.4.: a) Cable Attenuation b) LNA Gain

The gain of the amplifier is not stable and has a mean value of 15.6 dB. The gain stays between 16.6 dB and 14.8 dB, and is above 15.4 dB in the range of 11 – 16 GHz.

5.4.3. Data Correction

The original data collected in the measurements is converted into time-domain by using Fast Fourier Transform and is shown in figure 5.4.3.

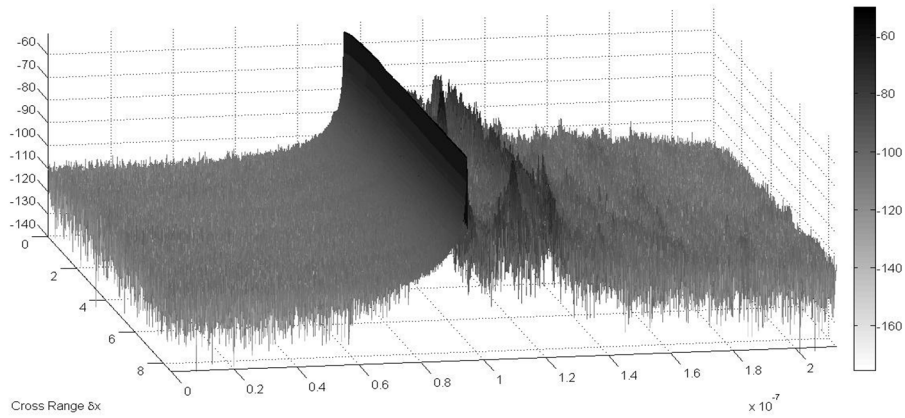


Figure 5.4.: Impulse response of Unprocessed SAR data

The first peak in the above figure is the direct component from transmit to receive antenna. The delay ahead of this peak corresponds to the propagation delay of the signal through the two 10 meter long coaxial cables, low noise amplifier, and small cables soldered to the antennas.

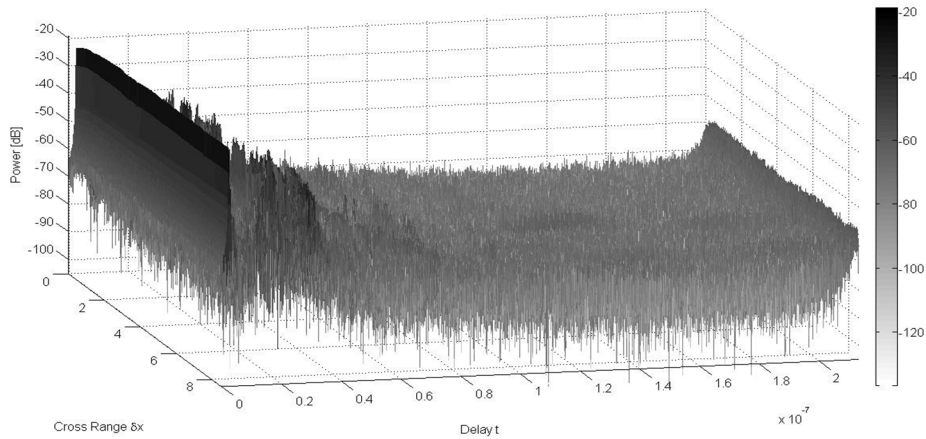


Figure 5.4.: Impulse Response after 20 meter long cable's effect removal

Impulse response, after removing the effect of two 10 meter long coaxial cables, is given in figure 5.4.4.

In the end, the effect of LNA and the cables soldered to the antennas is removed from S_{21} . The resulting impulse response is given in figure 5.4.5.

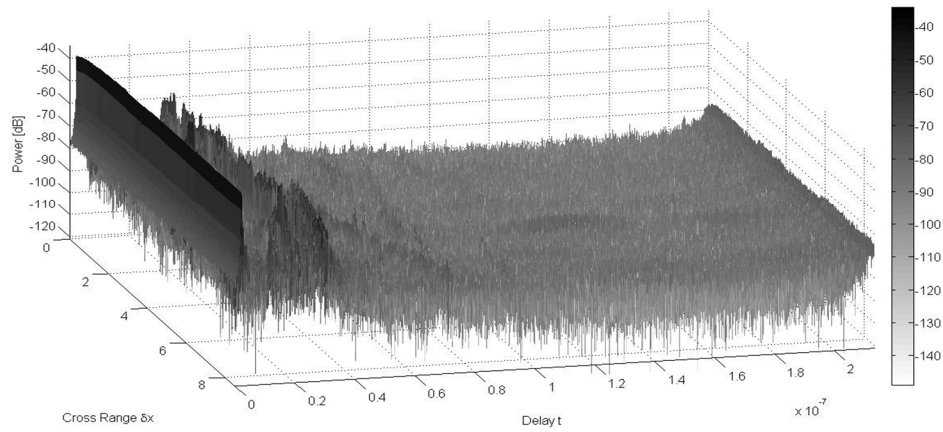


Figure 5.4.: Impulse response after full calibration

After all these corrections, the data can be used for generating the migrated image of the targets.

The corresponding transfer function after the calibrations is shown in figure 5.4.6. It is seen that as compared to figure 5.4.1, the signal loss at frequencies higher than 12.6 GHz has decreased from 30 dB to 10 dB after the calibration.

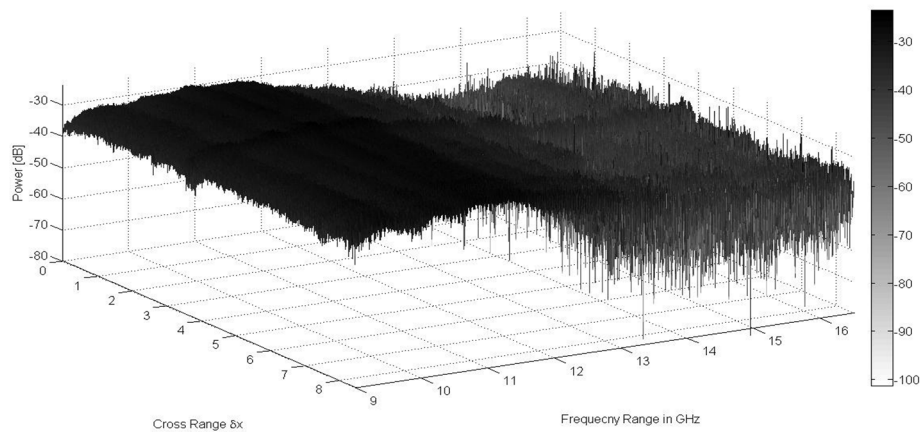


Figure 5.4.: Transfer Function after data correction

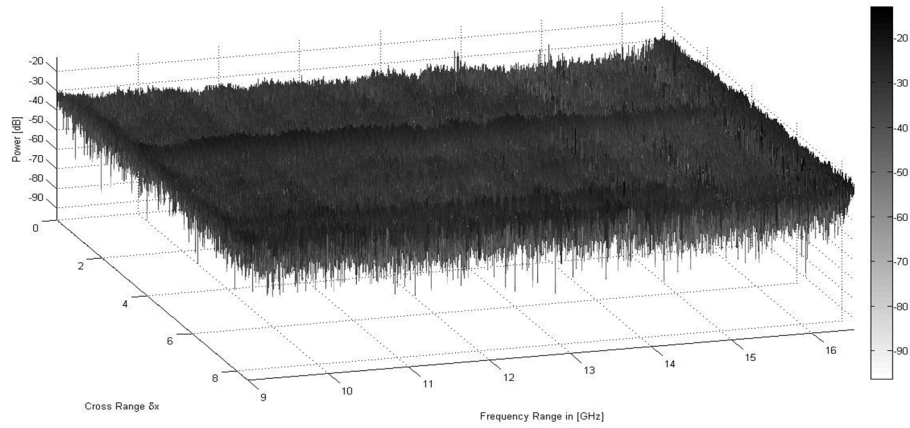


Figure 5.4.: Transfer function without direct antenna component

In order to see only the received power corresponding to the targets and their surroundings, the direct component of the antennas is removed from the corrected data; the resulting transfer function is given in figure 5.4.7. It is clearly seen that after the different data corrections and removal of direct component, the power received over the entire frequency band is around -35 to -40 dB.

Figures 5.4.3 to 5.4.7 are generated using measurement data of scenario 1 (details in chapter 6). Same correction steps are applied on the measured data of scenario 2 and 3 before using them in the algorithms.

Chapter 6:

6. Experimental Scenarios & Results

This chapter includes the three experimental scenarios and the resulting images migrated by the two selected migration methods; Diffraction Stack and Phase-Shift Method. The UWB radar system, explained in chapter 5, is used to measure the frequency domain data in the three different scenarios.

The setup of first two experimental scenarios was done in room E:2311 in EIT department of LTH, Lund University. The through-the-wall scenario setup was done in the wireless communications corridor in E building. The target objects selected for the measurements are metallic, thus having high reflectivity. We used one metallic plate, a metallic cylinder and a box wrapped in aluminum foil. The dimensions of the targets are given in table 6.1.

Object Name	Dimensions
Metallic Cylinder	Ø 11cm, H 30.5 cm
Metallic Plate	37 × 52 cm (L × W)
Aluminum wrapped Box	24 × 24 × 30 cm (L × W × D)

Table 6.1: Object Dimensions

As the height of the antennas on the trolley is approximately 140 cm, so we had to place the target objects at the same height to keep them in the same horizontal plane as the antennas. We used a table, 3 books, and 2 blocks to underneath the cylinder, 3 Tables for the metallic plate, and an iron stand to hold the aluminum wrapped box at the same height as the antennas, as shown in figure 6.0.1. As we used measuring tape for measuring the distance, there is a possibility of measurement error of up to ± 5 cm.

The first two scenarios are selected to test the accuracy of the migration algorithms and verification of selected system parameters, with the third being the main scenario as it involves EM wave-propagation through the wall.

Following sections contain the detail description of individual scenarios and the corresponding images generated by the migration algorithms.



Figure 6.0.: Target Objects for Scenario 1 & 2

6.1. Scenario 1: Description & Results

Measurements for scenario 1 are done in room E: 2311. Initial position of the antennas is taken as $[X_{ant} = 0.00, Z_{ant} = 0.00]$ and final position is at $[X_{ant} = 8.50, Z_{ant} = 0.00]$ meters with X and Z being cross range and down range respectively. The distance between antennas and the wall in front of them is 4.3 meters. This wall is not homogeneous, as it has two cabinets which are filled with metallic objects. The metallic Cylinder, metallic plate, and Aluminum wrapped box are placed at $[X_c = 0.95, Z_c = 3.00]$, $[X_p = 3.5, Z_p = 2.28]$, and $[X_b = 7.28, Z_b = 3.06]$ meters respectively. The complete scenario 1 layout with objects position relative to the antennas is shown in figure 6.1.1.

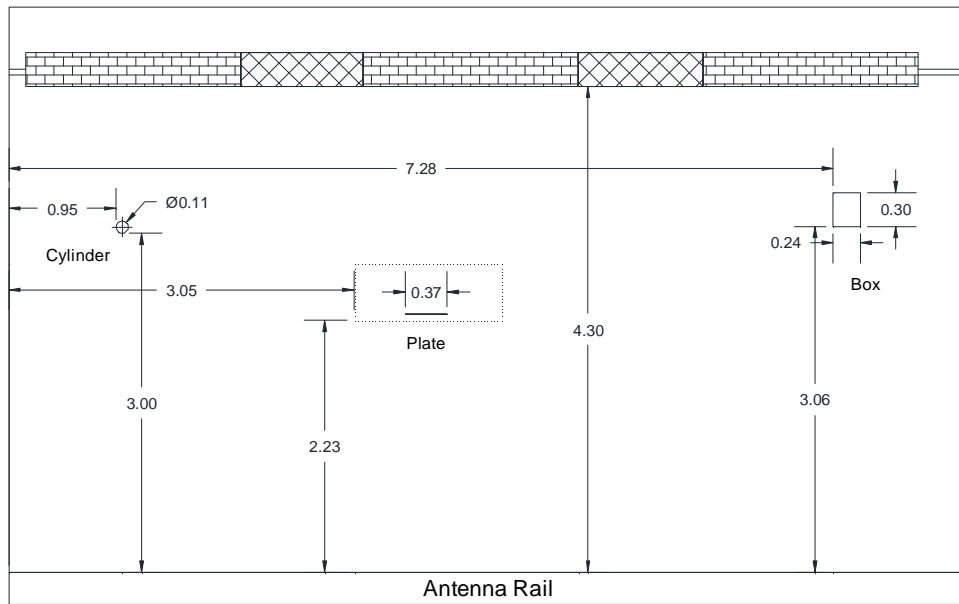
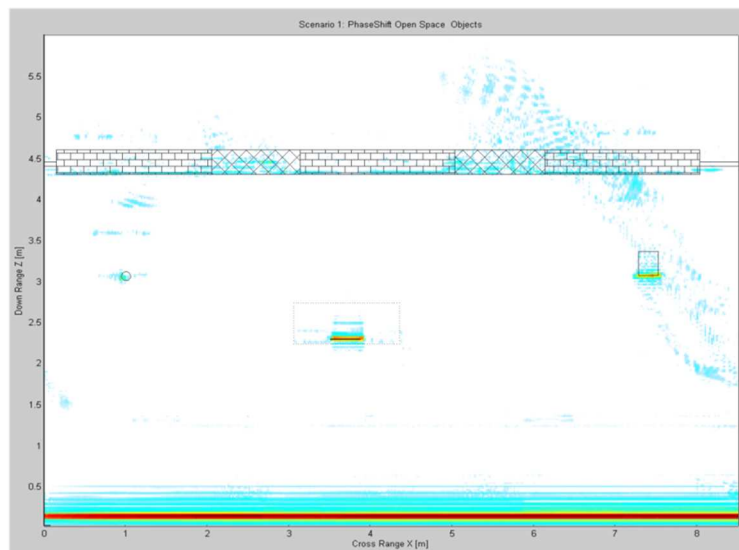


Figure 6.1.: Measurement Scenario 1 Layout

The results from Diffraction Stack (DS) and Phase-Shift (PS) migration algorithms are given in figure 6.1.2 a) and b) respectively.



a)

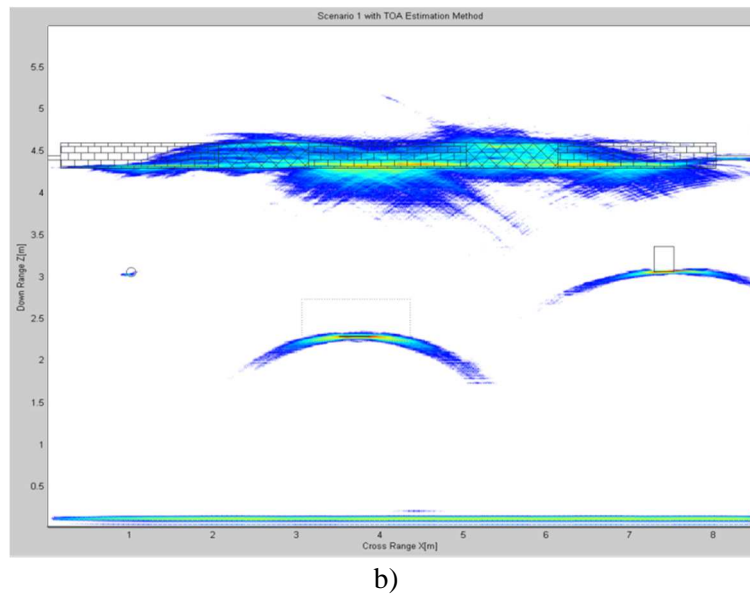


Figure 6.1.: a) Imaging results from Phase-Shift Algorithm, b) Diffraction Stack Algorithm

As it is clearly seen in figure 6.1.2, the side lobe levels of the DS migrated image are much higher than the image migrated by PS algorithm. This is expected as we also saw the same characteristics during the verification of the algorithms on the synthetic data. As a result, the dimensions of the target objects are much clearer in figure 6.1.2 a) with respect to b). As we did not place any absorbers between the antennas, there is a strong direct component at distance of 12 cm. It is seen that only the front of the box is clearly visible as most of the received energy is reflected by this surface and very little energy is received from the sides and back of the box.

In the figure 6.1.2, the cylinder's reflection signature is very low, corresponding to the fact that our SAR system is a forward looking system and due to its cylindrical shape, causing little energy to be reflected directly back towards the antennas and most of it to be scattered. There is a strong reflection from the front-wall. As the wall was not continuous, but had two wooden cabinets inside it, so, there were some strong reflections coming from inside the wall where cabinets are located, the reflections correspond to the presence of metallic objects in the wall cabinets. We are unable to see any distinct reflectors, which is due to the low received power from the reflections and due to being too close to each other with a distance less than 5 cm.

The clearest objects seen in figures 6.1.2 are the metallic plate and the aluminum wrapped box. Results achieved through PS algorithm give good information regarding the starting and ending point of the plate and the box with respect to cross-range with side-lobe levels of -21 dB and -28 dB respectively, with providing accurate down-range information with side-lobe levels of -12 dB. On the other hand, side-lobe levels in the results generated by DS algorithm are mere -4 dB, so we cannot find the starting point of both plate and the box with good accuracy. Nevertheless, they give good accuracy about the location of the objects in down-range.

Apart from the placed target objects, we see many artifacts in the radar images generated by the phase-shift method (also seen when using noise-free synthetic data) which results from the use of fast Fourier transform instead of discrete Fourier transform as described by the authors in [16].

6.2. Scenario 2: Description & Results

In scenario 2, we have investigated the effects of two closely spaced targets on the migrated image. E: 2311 was used for this scenario. Here we placed the metallic cylinder in front of the metallic plate at a distance of 57 cm at the coordinate's $[X_c = 3.63, Z_c = 1.71]$ meters as shown in figure 6.2.1. The aluminum wrapped box is not moved for this measurement scenario. The complete scenario 2 layout is given in figure 6.2.2.



Figure 6.2.: Cylinder in front of Plate in Scenario 2

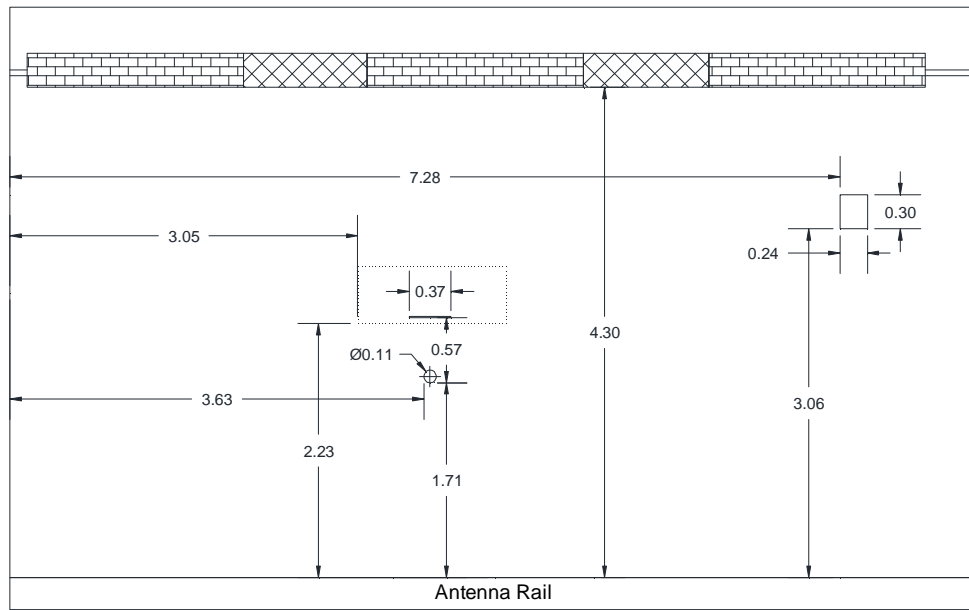
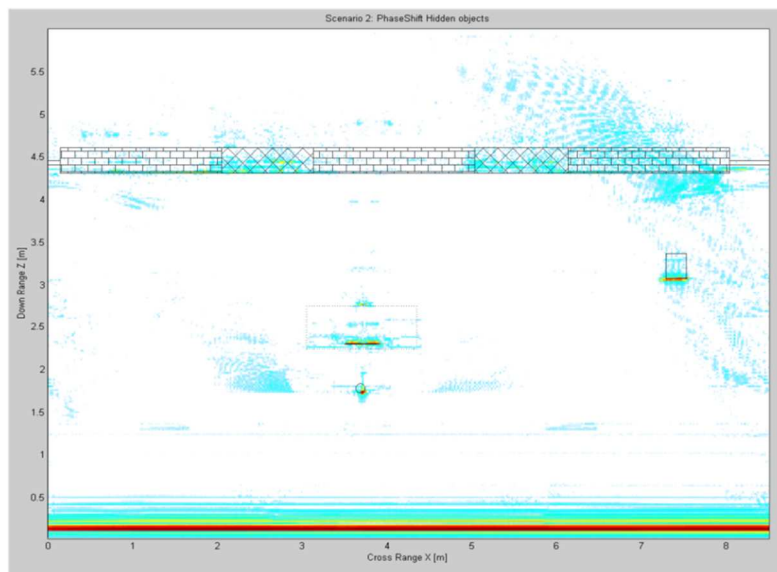


Figure 6.2.: Measurement Scenario 2 layout

The resulting migrated images from both algorithms are given in figure 6.2.3.



a)

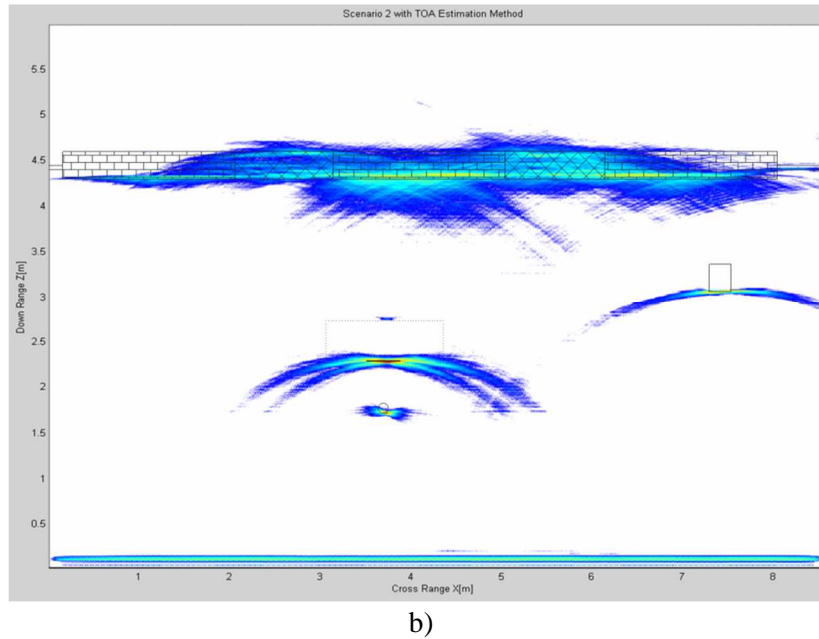


Figure 6.2.: a) Image generated by Phase-Shift Algorithm, b) Image generated by Diffraction Stack Algorithm.

The images generated by both the algorithms are quite accurate in regenerating and positioning the target objects at their correct locations. As mentioned before, the side lobe level of DS is much higher than PS, thus we can extract less information about the dimensions of the target from figure 6.2.3 b) as compared to figure 6.2.3 a). Another interesting thing seen is that the portion of the plate directly behind the cylinder is not visible as clearly as the rest of the plate which can be attributed to the forward looking nature of our radar system. There are some strong artifacts behind the plate at a distance of approximately 44 cm. The distance between plate and the rear of the cylinder is approximately 46 cm. According to our calculations, this is caused by the reflections of the waves between plate and cylinder i.e. a wave arrives at the plate, gets reflected towards the cylinder, cylinder reflects it back towards the plate, and finally the wave gets reflected again from the plate and reaches the receive antenna. Or we can say that for this frequency range the plate acts as mirror for the cylinder, so there is an inverted mirror image of the cylinder. Yet again, the aluminum wrapped box is shown at its exact location and the reflections from the cabinets are also seen here.

6.3. Scenario 3: Description & Results

In this scenario, we investigated the effects of presence of a wall between the antennas and the targets on the migrated image generated by the two algorithms. In ideal conditions, the wall should be homogeneous and its relative permittivity ϵ_r should be known so that the wall compensation can be done with good accuracy. But in practical cases, the wall is never homogeneous and as a result, the properties of the materials are not known. In order to get accurate results, we made approximations regarding the permittivity and width of the wall.

Measurements for scenario 3 were done in office corridor of the wireless department at EIT building, LTH, Lund University. Antennas were at a distance of approximately 44 cm from the wall. A portion of the wall was made up of plaster and bricks and another portion was made from concrete with reinforced metallic grid in side of the wall. There were also 3 wooden doors in front of the antenna aperture. Our 9 meter rail covered 3 offices of the corridor.

We placed the metallic plate inside room 1 and the metallic cylinder inside room 2 as shown in figure 6.3.1. These are placed directly behind the wooden door. The dimensions of the rooms are 4×6 meters. As we did not have access to room 3, we could not place a target inside it.

Figure 6.3.2 shows the rail assembly and the antennas setup in the corridor.



Figure 6.3.: Metallic Plate and the cylinder placed in two different rooms

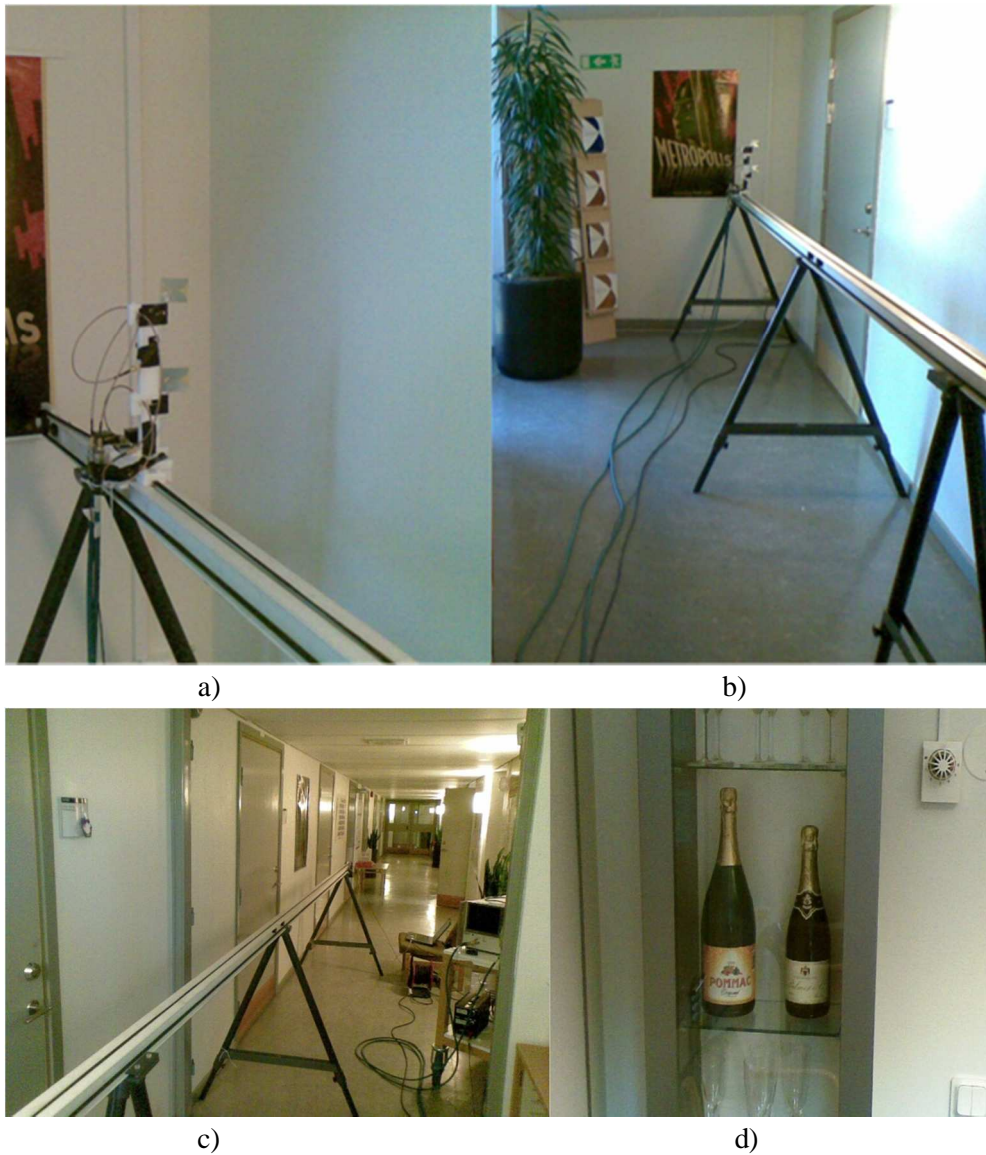


Figure 6.3.: a) Antenna Assembly, b) & c) 9 meter long rail covering 3 offices, along with the VNA and Laptop, d) wooden cabinet with two bottles inside room 1

The complete scenario layout with distance measurements is given in figure 6.3.3. Here, antenna's starting position is $[X_{ant} = 0, Z_{ant} = 0]$ meters, the position of metallic plate is approximately $[X_p = 0.60, Z_p = 2.60]$ meters, and the metallic cylinder is placed at approximately $[X_c = 3.93, Z_c = 1.64]$ meters. The contents of the room 3 are unknown.

The width of the plaster wall and the doors is approximately 12 cm, and 4 cm respectively. The width of the concrete wall is unknown (~15 cm).

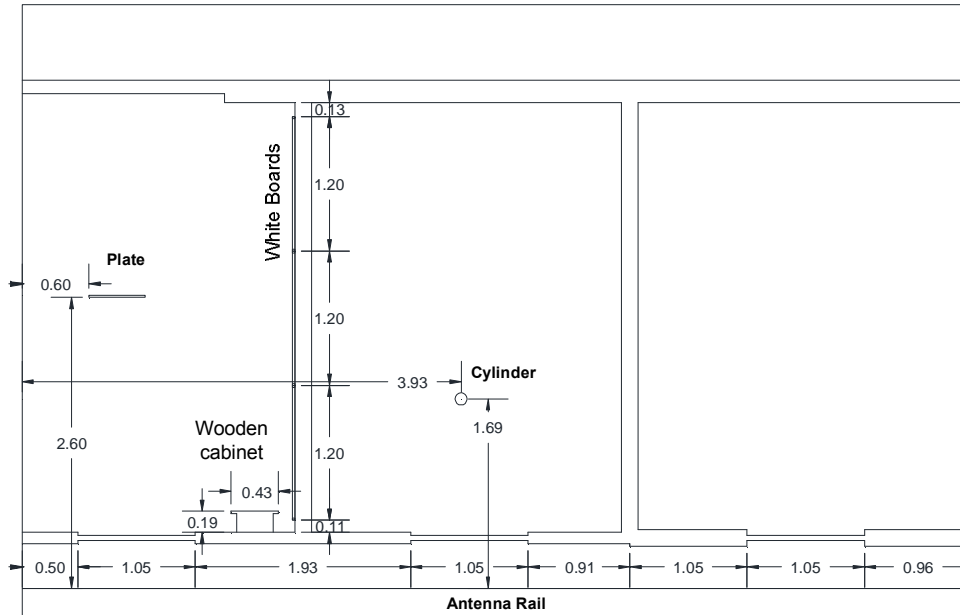


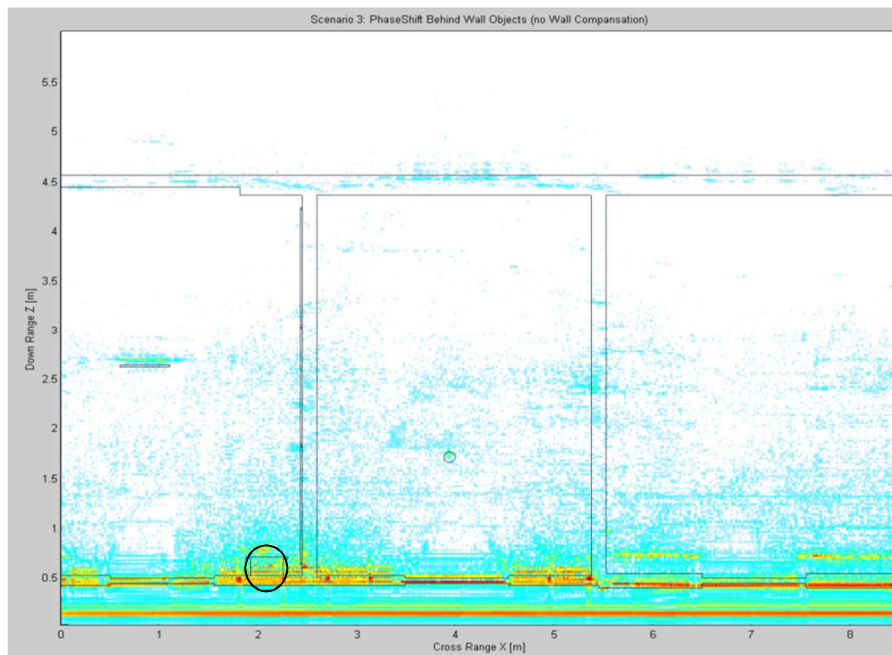
Figure 6.3.: Scenario 3 Layout

6.3.1. Results without wall compensation

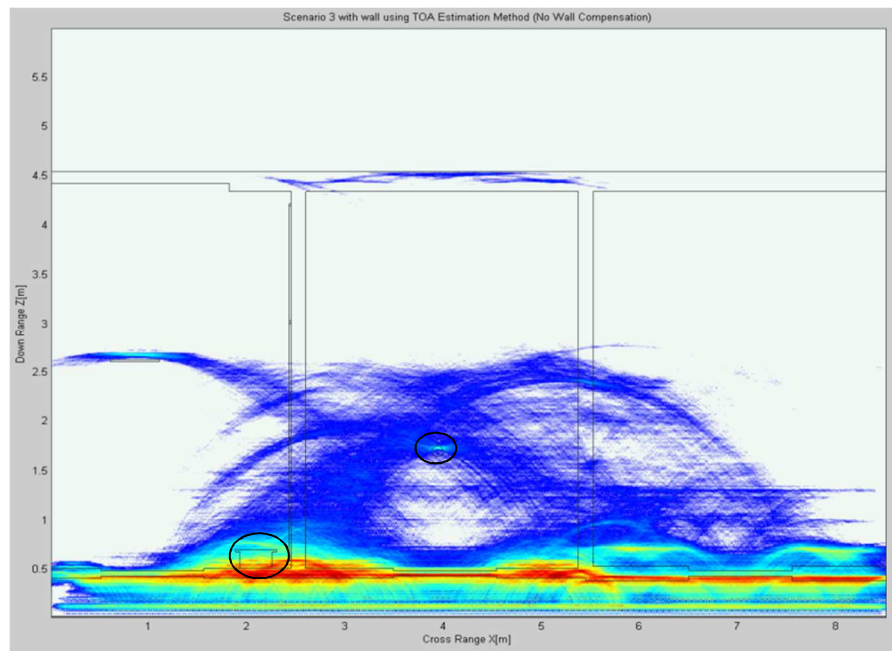
This section contains the migrated images generated by Diffraction Stack (DS) and Phase-Shift (PS) algorithms without taking into account the effects of the wall. As expected, target positions are not shown at their original locations, rather they are shown approximately 8 cm away from their true positions. This is due to the change in velocity of the wavefield inside the wall. As clearly visible, the side lobe level produced by DS algorithm is much higher than PS algorithm. As a result, the image generated by PS algorithm is giving us much more information about the target objects present.

As the rooms were not entirely empty, so instead of just having the reflection from the target objects, we also have a lot of reflections from the other objects present inside the room.

The results without wall compensation are shown in figure 6.3.4.



a)



b)

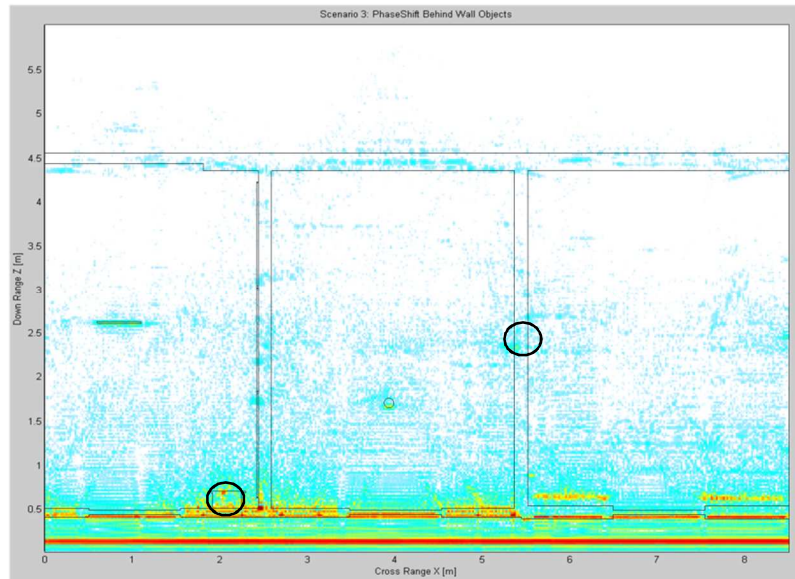
Figure 6.3.: Scenario 3-without wall compensation
a) Phase Shift results b) Diffraction Stack results

In figure 6.3.4 a), if we look closely at the wall, we see the presence of several strong reflectors at the center of the wall which could be metallic studs placed approximately 44 cm apart. These metallic studs are not visible in b) which is due to higher side-lobe levels generated by DS algorithm. Metallic studs are only seen in the plaster wall, whereas, a strong continuous reflector is seen in the concrete wall starting at 5.5 meters which probably corresponds to reinforced metallic structures present inside the wall.

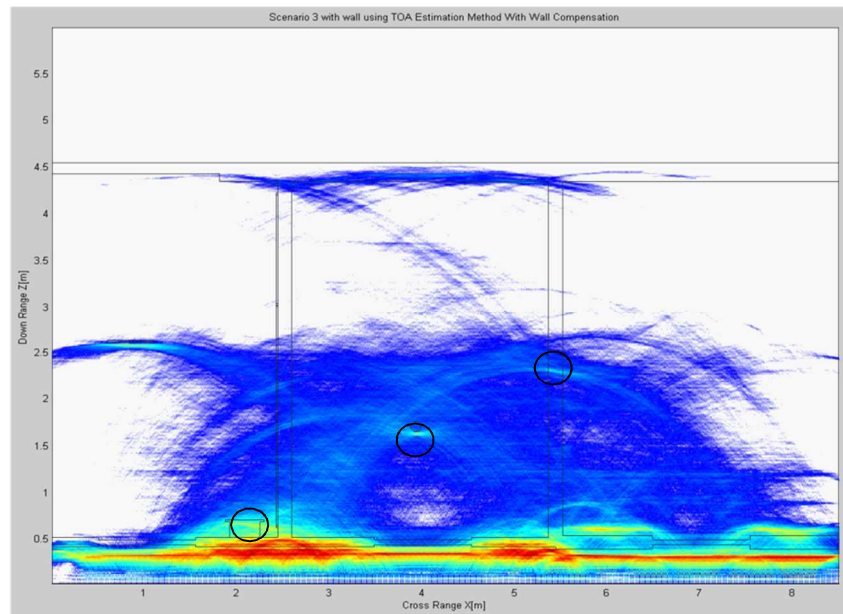
In figure 6.3.4, we can see strong reflection from inside the wooden cabinet in room 1 with two distinct peaks in a) and a common peak in b). This could correspond to the bottles present inside the wooden cabinet as shown in figure 6.3.2 d). There are also two strong reflections right next to the wall of room 3 which are clearly seen in both images. We did not find any reflecting object placed at that range in the room 3. These reflections could be generated by the other side of the wall and as the wave speed inside concrete is less than that of plaster, the reflections are shown outside the width of the wall.

6.3.2. Results with wall compensation

As described in section 6.3.1, in order to correctly compensate for the effects of the wall, the wall should be homogeneous (same building material), the exact thickness of the wall should be known, and the relative permittivity ϵ_r should be known beforehand. In practical scenarios, wall-thickness, material of the wall, and the permittivity of the material is never known, also, the walls are not homogeneous and are made up of different type of materials ranging from concrete, bricks, metallic studs etc. So, we have to do approximate the width and permittivity of the wall. An error in these approximations will only result in the shift in target location along Z axis i.e. the targets will not be at their true positions, with the symmetry in the target's shape intact. In our case, the wall is not homogeneous; the width is not same due to the presence of the doors, width of the wall is 12 cm and the door width is 5 cm.



a)



b)

Figure 6.3.: Wall Compensated Images. a) Image Generated by Phase-Shift Method b) Image Generated by Diffraction Stack

As an approximation, we took width of the wall as 10 cm and the relative permittivity ϵ_r of the wall as approximately 4.1 (ϵ_r for concrete is 4.5). These values were used to generate the migrated images which are given in figure 6.3.5.

By using the approximations, we were able to get the correct locations of the targets with less clutter in the PS generated image as compared to the DS image. We can also see one strong reflection from an object from inside the wooden cabinet in figure 6.3.5 a), we assume that it could correspond to one of the bottles having a golden foil wrapped around it as shown in figure 6.3.2 d), we are not sure about this as there was no object present right in front of the cabinet. However, the two peaks seen in figure 6.3.4 a) have moved towards the inside of the wall. This strong reflection is not seen in the figure 6.3.5 b) as there is a lot of clutter at the location of the cabinet. Also, seen in both the figures, the reflections from the opposite wall are quite clearly visible in figure 6.3.5 a) whereas only the opposite wall of the middle room is visible in figure 6.3.5 b). In figure 6.3.5 a) there are some reflections from the side walls of the room 1 corresponding to the metallic frame of the white board. The metallic studs are also visible inside the wall, though they have moved a bit closer towards the antennas resulting from the wall compensation. The metallic studs, as well as, the reflections from the side wall of room 1 are not visible in figure 6.3.5 b). There is another strong reflection coming from the wall between room 2 and room 3 at a distance of 2.4 meters from the antennas. It could correspond to the metallic holders holding the book shelves present in both the rooms, but we are not sure.

There are two strong reflections right next to the wall of room 3 which are clearly seen in both figures 6.3.5 a) and b). We did not find any reflecting object placed at that range in the room 3. These reflections could be generated by the other side of the wall. After the wall compensation, these reflections did not move inside the wall, this is not surprising as we did not compensate for the concrete wall.

The results for different ϵ_r and different wall width are given in Appendix A.

6.4. Results for Small Bandwidth

As said in section 5.4, the received power S_{21} component was decreasing after frequency range of 12.6 GHz, but the received power from the targets and their surroundings was -35 to -40 dB, so in this section we are going to present images generated using two frequency ranges, i.e. 9 – 12.5 GHz (3.5 GHz bandwidth) and 12.5 – 16.5 GHz (4 GHz) and discuss the implications on the theoretical and achieved resolution of the migrated images. Table 6.2 contains the information about the achieved and theoretical resolutions achieved by these two

frequency bands. These values are chosen after analysis of images generated for scenario 1.

Migration Techniques	Frequency Range	Cross Range [cm]		Down range [cm]	
		Theoretical	Practical	Theoretical	Practical
Phase Shift Algorithm	9 - 12.5 GHz	1.4	2	4.3	6
	12.5 - 16.5 GHz	1	2	3.7	6
	9 – 16.5 GHz	1.2	2	2	2
Diffraction Stack	9 - 12.5 GHz	1.4	≥6	4.3	4
	12.5 - 16.5 GHz	1	≥5	3.7	4
	9 – 16.5 GHz	1.2	≥6	2	2

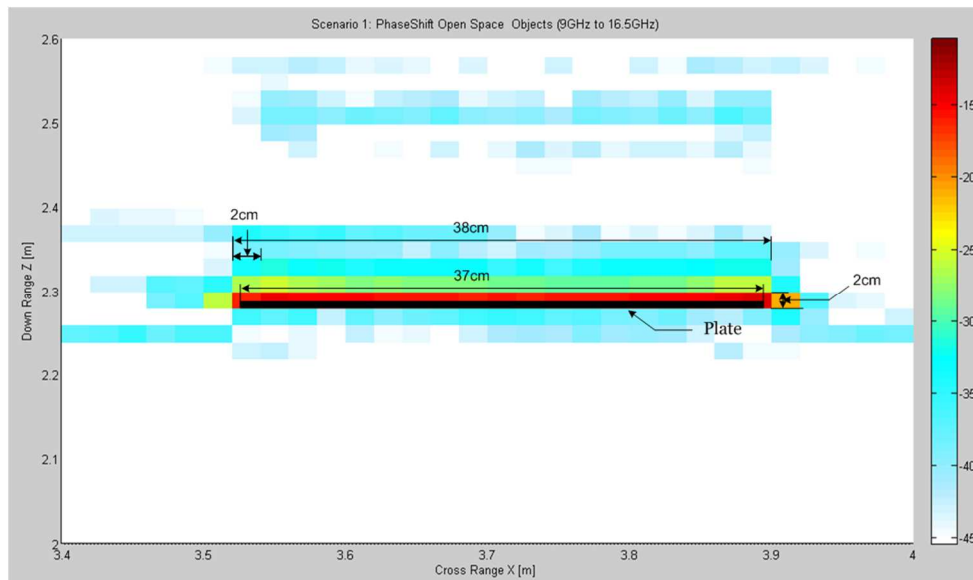
Table 6.2: Image Resolutions for different frequency ranges

The theoretical cross and down range resolutions are found by using eq. (5.6) and (5.7). As given in table 6.2, the practical image resolution achieved by the radar system when using lesser bandwidth is less than the theoretical resolution and the resolution achieved when using full bandwidth. This is due to the rise in side lobes in the images generated by both algorithms, with DS resulting in better resolution in down range and PS resulting in better resolution in cross range.

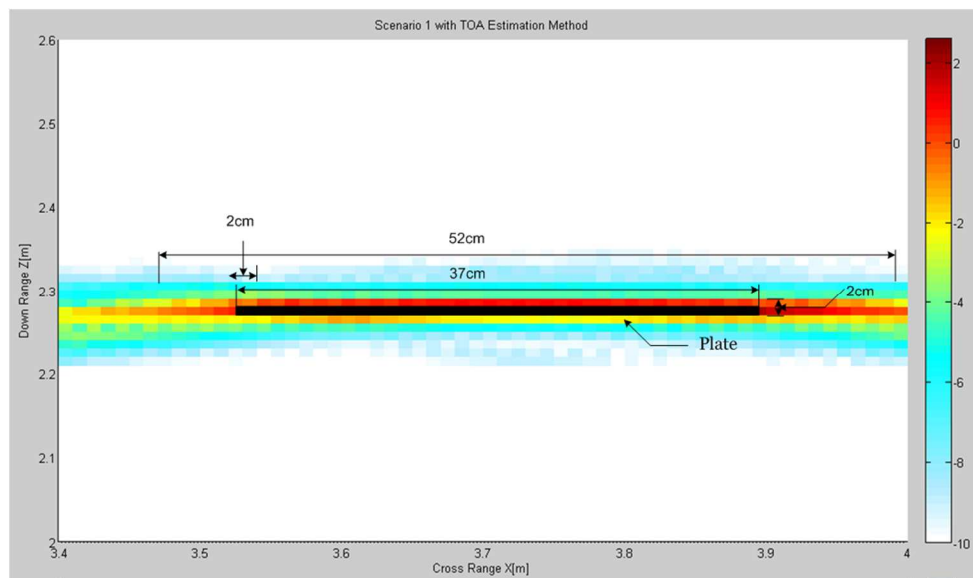
$$\delta z = \frac{c}{2 \times B} \quad (5.6)$$

$$\delta x = \frac{c \cdot Z}{2 \cdot f_c \cdot X} \quad (5.7)$$

The figures 6.4.1 to 6.4.3 are showing the practical resolution achieved for the scenario 1 by Phase-Shift method and Diffraction Stack Algorithm. The images are zoomed onto the metallic plate placed in front of the antenna rail in scenario 1.

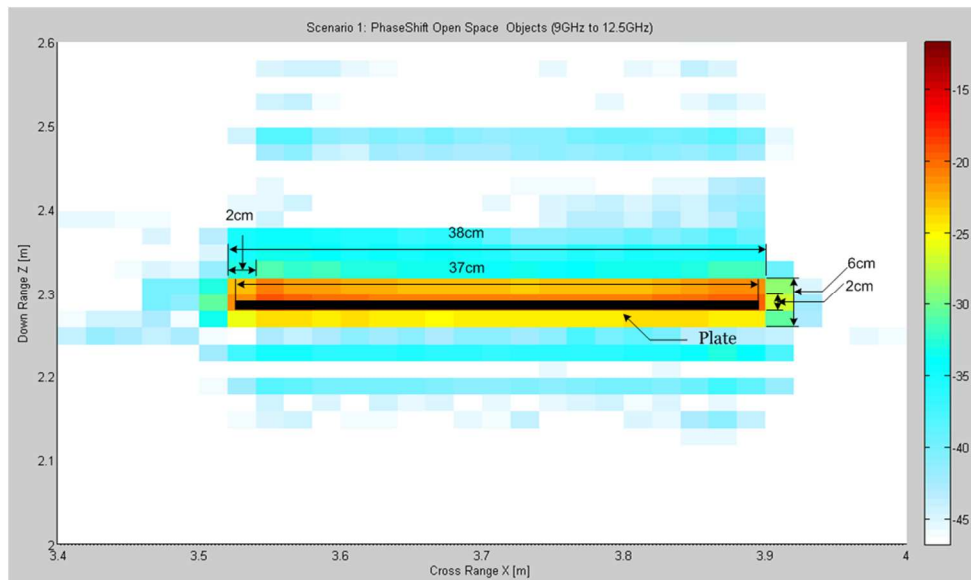


a)

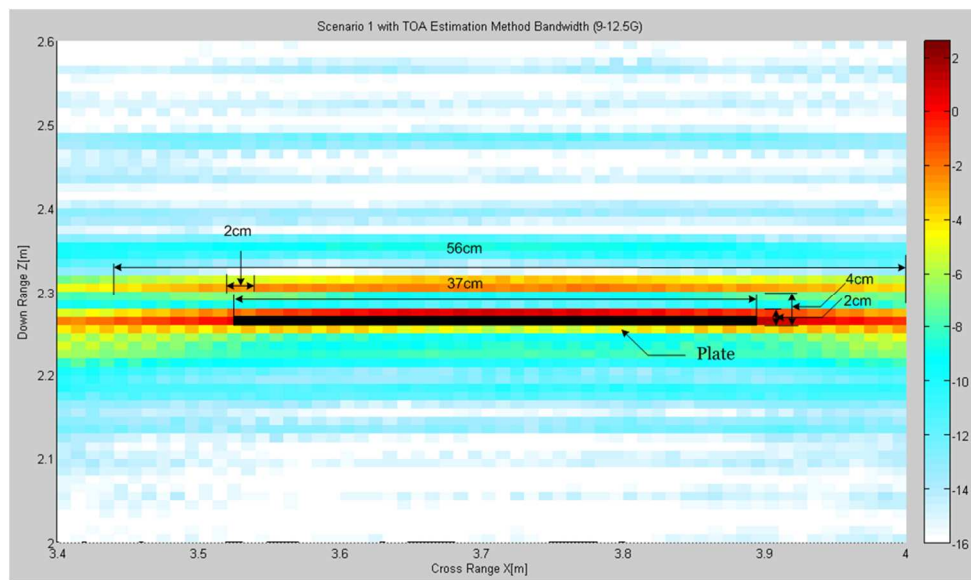


b)

Figure 6.4.: Practical Resolution using full 9 – 16.5 GHz
 a) Phase-shift Method b) Diffraction Stack Algorithm

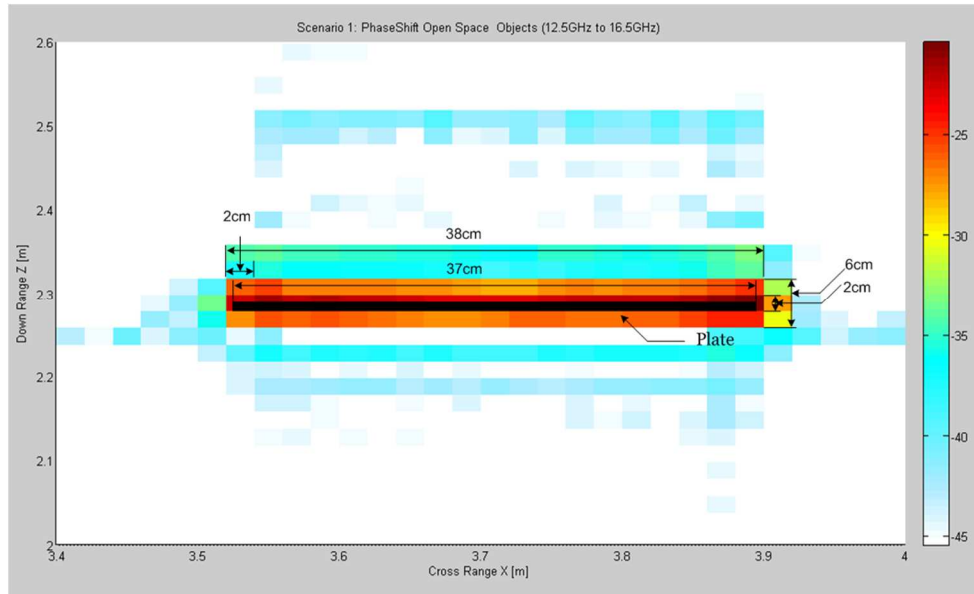


a)

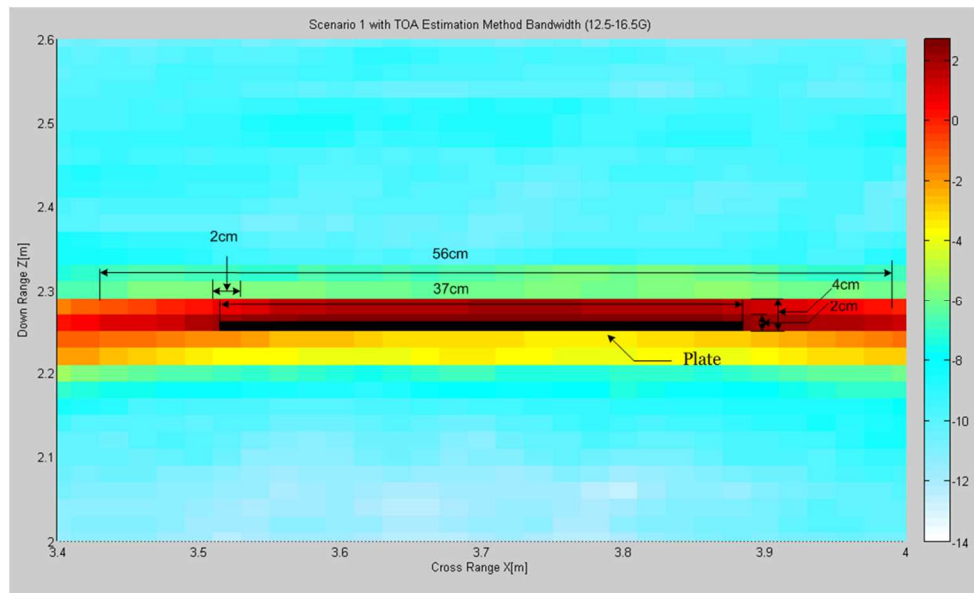


b)

Figure 6.4.: Practical Resolution using 9 – 12.5 GHz
 a) Phase-shift Method b) Diffraction Stack Algorithm



a)



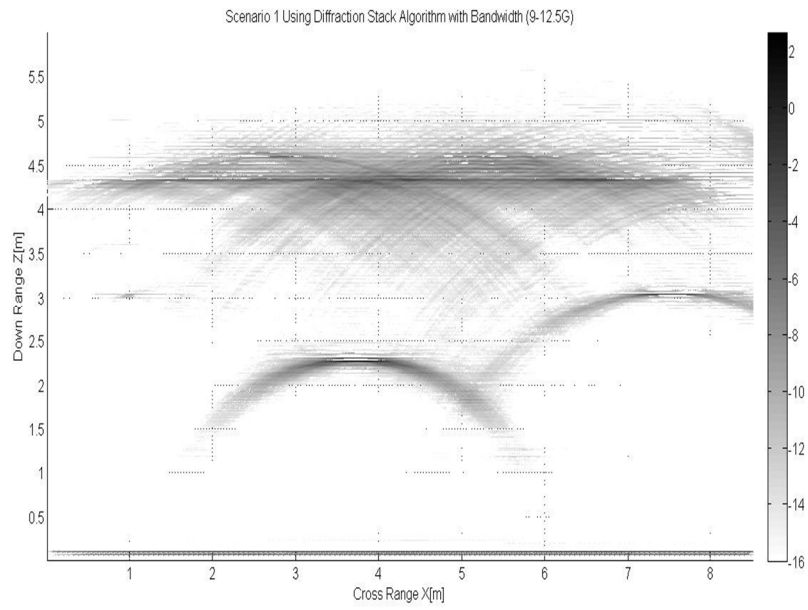
b)

Figure 6.4.: Practical Resolution using 12.5 – 16.5 GHz
 a) Phase-shift Method b) Diffraction Stack Algorithm

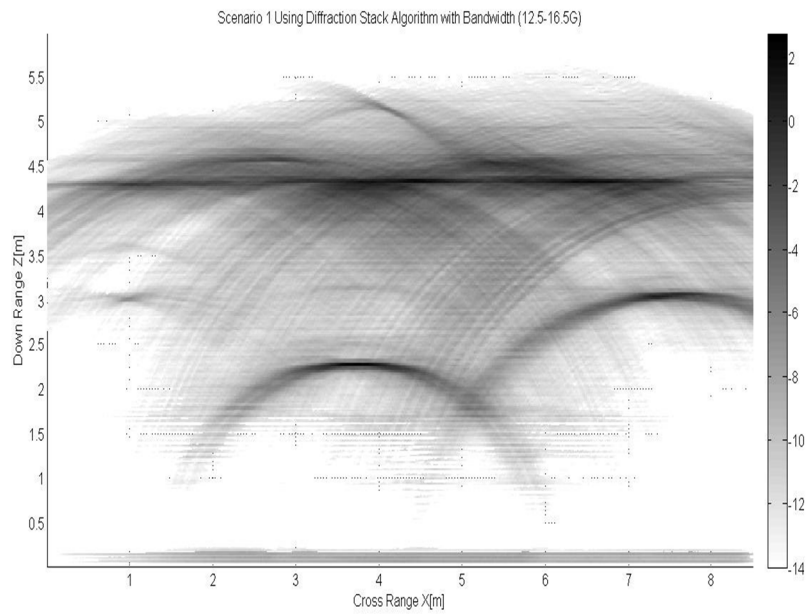
Images generated using the above two frequency bands are shown in the figures 6.4.4 – 6.4.9. As seen clearly, the resolution of the generated images is worse than the images generated using full bandwidth, which was expected. The figures generated using the frequency band of 9 – 12.5 GHz are giving somewhat clearer results as compared to images generated using 12.5 – 16.5 GHz. This could be due to the lower signal to noise ratio at higher frequencies.

The power in the direct component present in the received signal as seen in figures 6.4.4 – 6.4.9 is less in the frequency range of 12.5 – 16.5 GHz as compared to the lower frequency range. This is due to the fact that the directivity of the Vivaldi antennas used increases with increasing frequency.

Following are the figures generated using the two different frequency ranges.

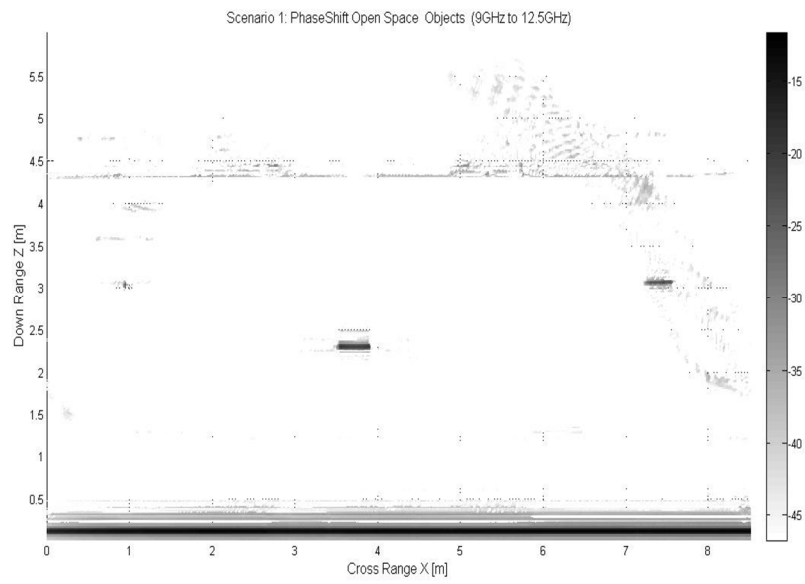


a)

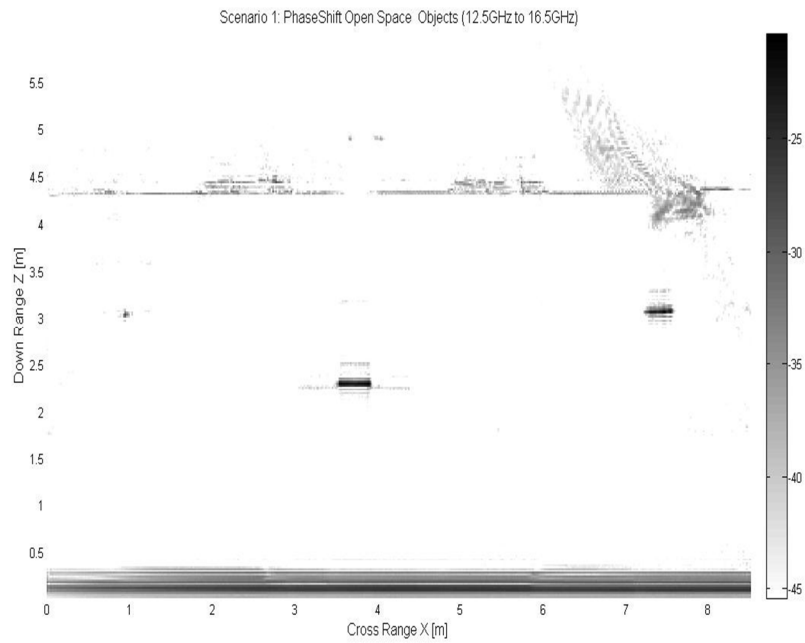


b)

Figure 6.4.: DS results for Scenario 1 using different frequency ranges
a) 9 - 12.5 GHz b) 12.5 - 16.5 GHz

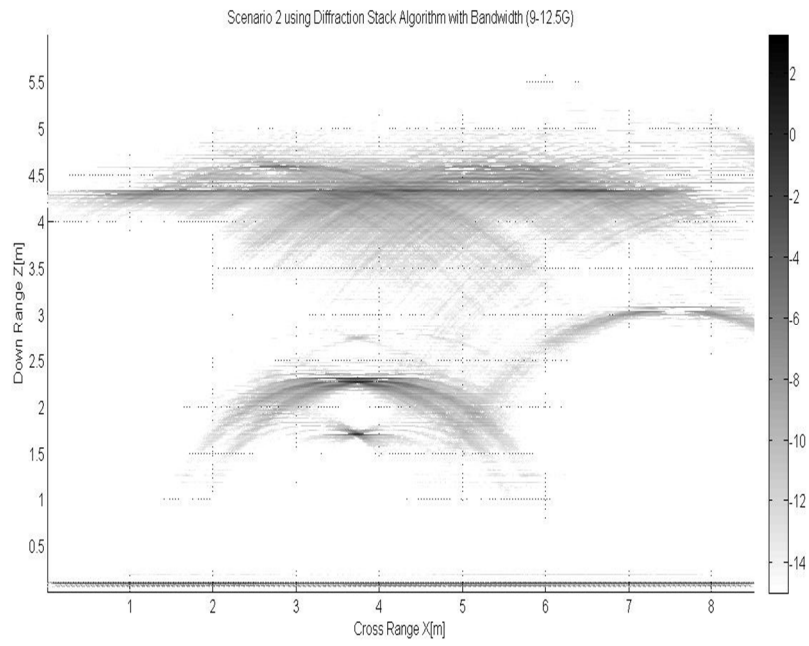


a)

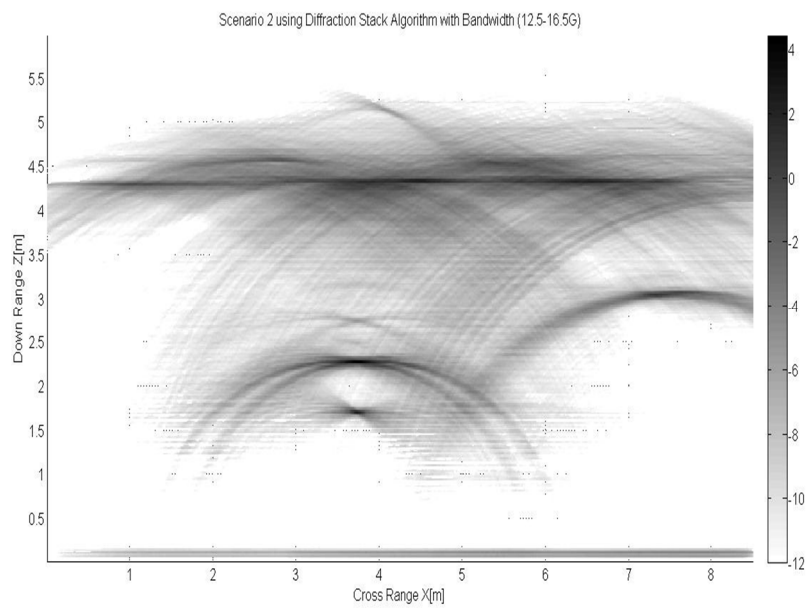


b)

Figure 6.4.: PS results for Scenario 1 using different frequency ranges
a) 9 - 12.5 GHz b) 12.5 - 16.5 GHz

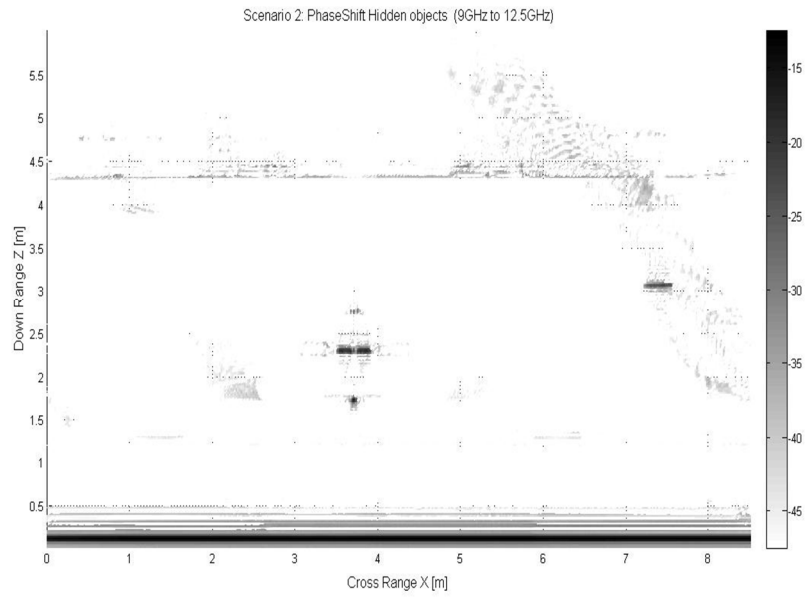


a)

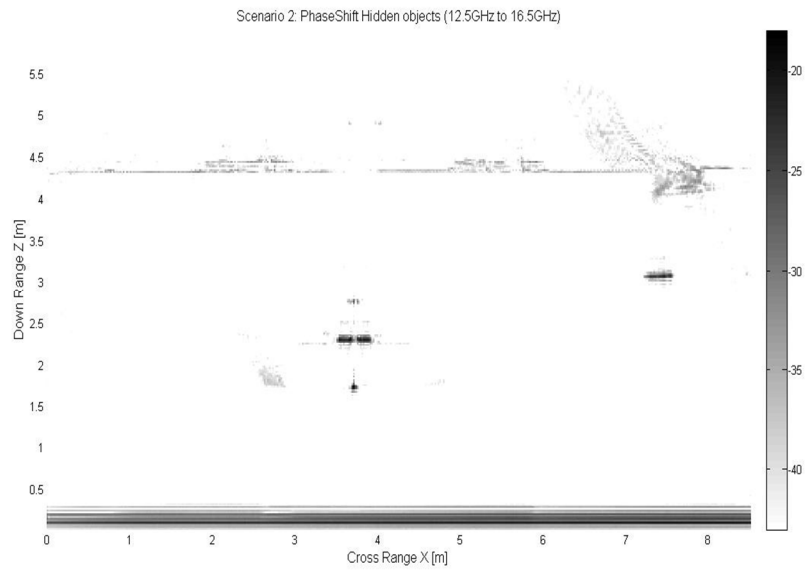


b)

Figure 6.4.: DS results for Scenario 2 using different frequency ranges
a) 9 - 12.5 GHz b) 12.5 - 16.5 GHz

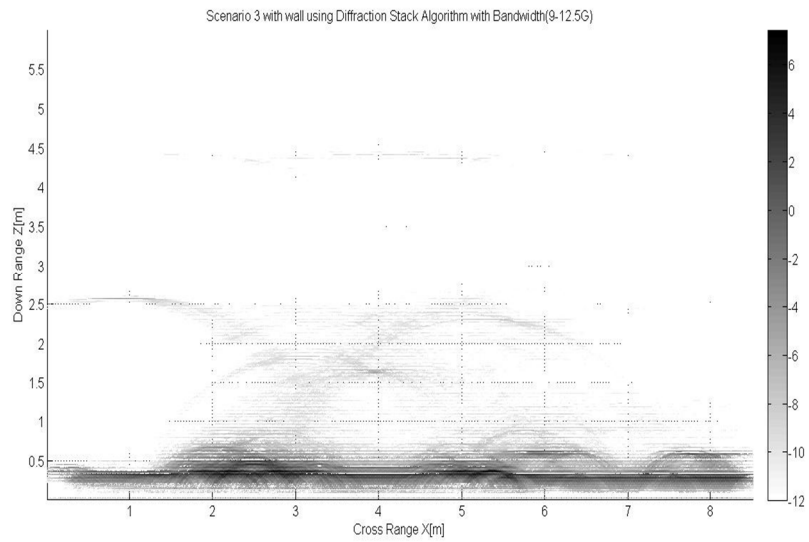


a)

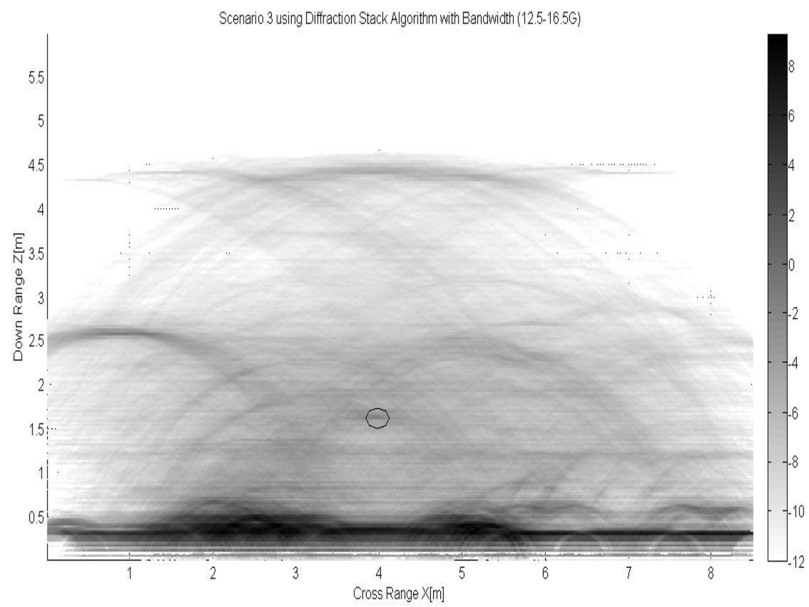


b)

Figure 6.4.: PS results for Scenario 2 using different frequency ranges
a) 9 - 12.5 GHz b) 12.5 - 16.5 GHz

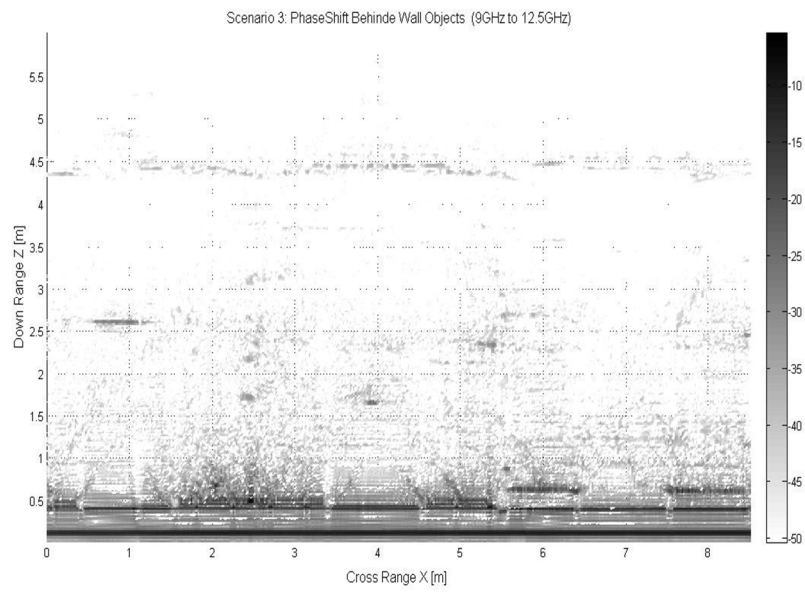


a)

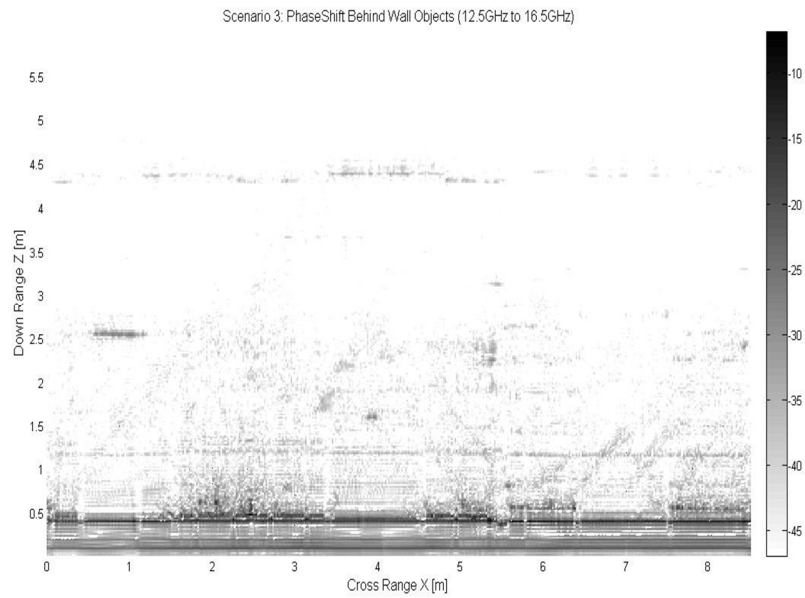


b)

Figure 6.4.: DS results for Scenario 3 using different frequency ranges
a) 9 - 12.5 GHz b) 12.5 - 16.5 GHz



a)



b)

Figure 6.4.: PS results for Scenario 3 using different frequency ranges
a) 9 - 12.5 GHz b) 12.5 – 16.5 GHz

Chapter 7:

7. Conclusions & Future Work

7.1. Conclusions

The goal of this master's thesis project was to use the Ultra Wideband signals to locate objects placed behind a wall. Two migration algorithms were selected aiming to show two completely different approaches to transform the measured data into a 2-D image showing the true positions of the targets. The methods are Phase-Shift method using scalar wave equation and Diffraction Stack algorithm using geometrical approach. Measurements were done through a Synthetic Aperture Radar technique using a total of 8.5 meter synthetic aperture in the frequency range of 9 – 16.5 GHz. The effects of cables and LNA were then removed from the data. The received power was however not constant over the entire bandwidth with power level staying at -45 dB up till 12.6 GHz and then decreasing to a level of -55 dB at 16.5 GHz. This was caused by the strong direct component present in the received signal. However, this effect did not cause any problem and both algorithms were able to generate the images with good accuracy.

Both algorithms were able to migrate the data back to their true spatial positions, but the generation of high side-lobe levels around the reflectors by the DS algorithm caused a loss of information about the environment, whereas, the Phase-Shift migration algorithm gave best image quality, very low side-lobe levels and was able to extract much greater information about the environment. Also, the simulation time of DS algorithm was around 20 minutes whereas the PS algorithm generated the results in mere 1.5 minutes. However, the theory and implementation of the DS algorithm were very much straight forward as compared to PS algorithm which involved scalar wave equation. For both the cases, the correct information about relative permittivity of the wall, ϵ_r , and width of the wall, L_w , should be known in order to move the objects back to their correct positions.

After taking into account the image results, error margins, side-lobe levels, image resolution and the computational time required by both the algorithms, we

concluded that PS algorithm is a much better solution for data migration due to sheer speed of execution and the ability to extract extra information about the channel (metallic studs inside the wall).

7.2. Future Work

In this section we will explore the possibilities of future work which can be done. One interesting aspect could be to find the optimal bandwidth and frequency range which results in higher received power levels in through-the-wall scenarios, consequently resulting in longer range and better visibility of the targets.

Another interesting aspect could be to investigate the effects with materials like rubber, plastic, clothes or other non-metallic materials which could be very useful especially at the airports for scanning the baggage as an additional tool to the current x-ray scanners.

In practical scenarios, the “time” is the main constraint on the UWB radar systems. The “time” includes the measurement time and the time taken by migration algorithm to process the data and generate a radar image. The measurement time could be reduced by reducing the aperture length and increasing the antenna step size Δx . In order to reduce the processing time of the migration algorithms, special digital signal processing kits could be developed which will result in significant reduction in the computational time taken by the migration algorithms for radar image generation.

Another interesting research area could be to use 2D imaging methods to generate a 3D image. The 3D environment response could be measured by replacing the Rx antenna with a vertical antenna array. In this way, the complete geometry of the target could be identified.

One very interesting research task could be to implement a system based on a mobile robot i.e. placing antennas on a remote controlled car and then measuring the environment by moving the car around the target area, resulting in a very portable radar system. The main task for such a system will be the development of a transponder module for transmitting, receiving, and storage of the measured data. Additionally another module could be used to transmit this data to a nearby computer where the imaging algorithm could be applied to the data and radar images could be generated.

Appendix

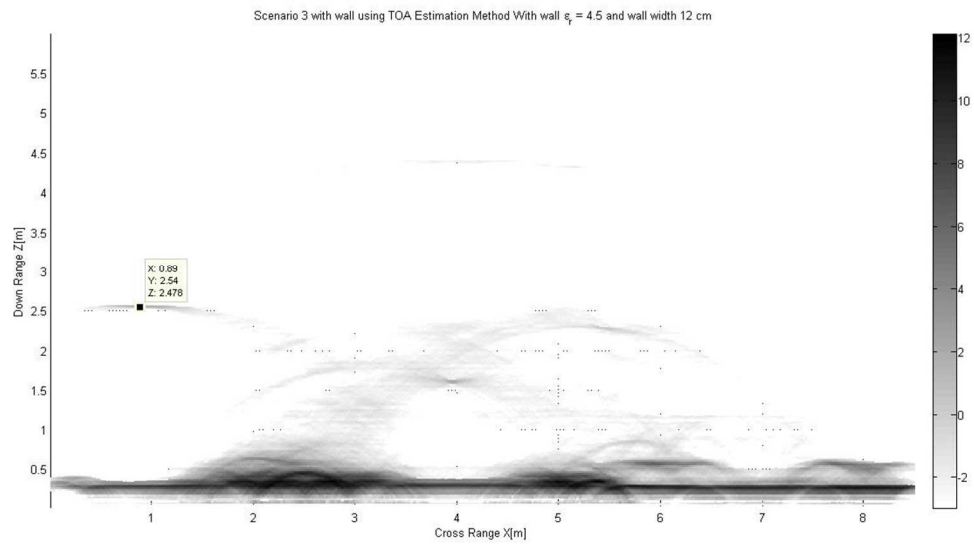
A.Results with different ϵ_r and wall width

Table A.1 contains the values of relative permittivity and width of the wall used to generate the images and the resulting error in position estimation of target objects.

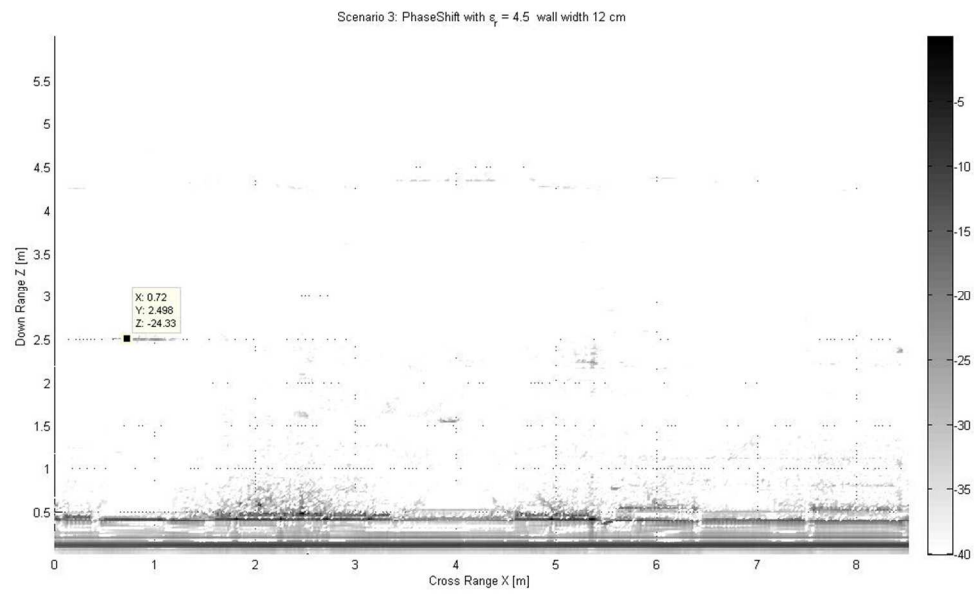
Medium Type	Parameters		Error in location	
	ϵ_r	L_w [cm]	Diffraction Stack	Phase Shift
Concrete Wall	4.5	12	2.5 %	4 %
Wall (Plaster with Bricks)	4.95	12	3 %	5 %
Wooden Door	2.83	4	2 %	1 %

Table A.1: Error in Position Estimation due to different parameters

The results seen when using parameters for the wood give the next best results with respect to approximated parameter values. It could correspond to the fact that the target objects were placed exactly in front of the wooden doors, so most of the energy is received by the antennas when they were directly in front of the wooden door.

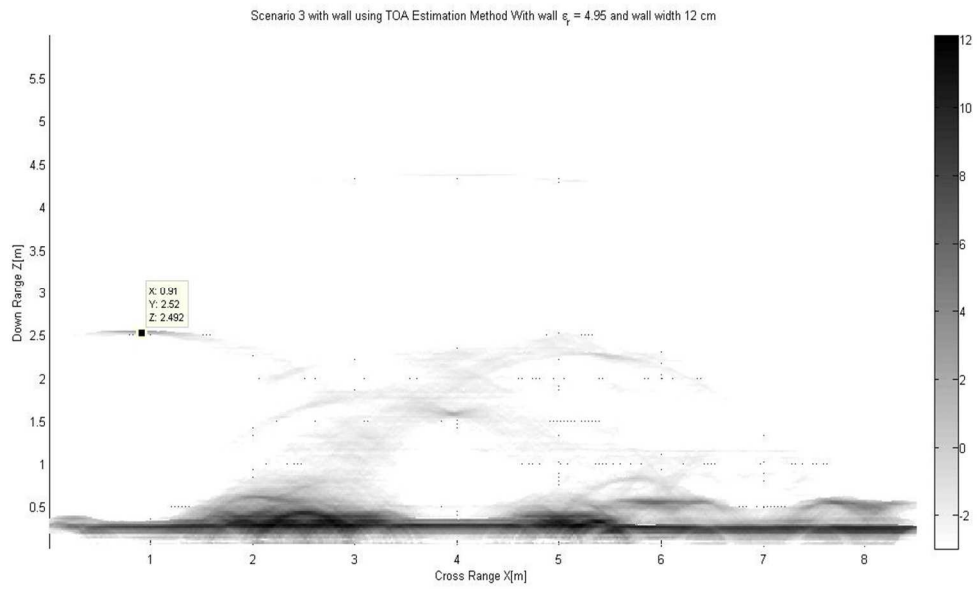


a)

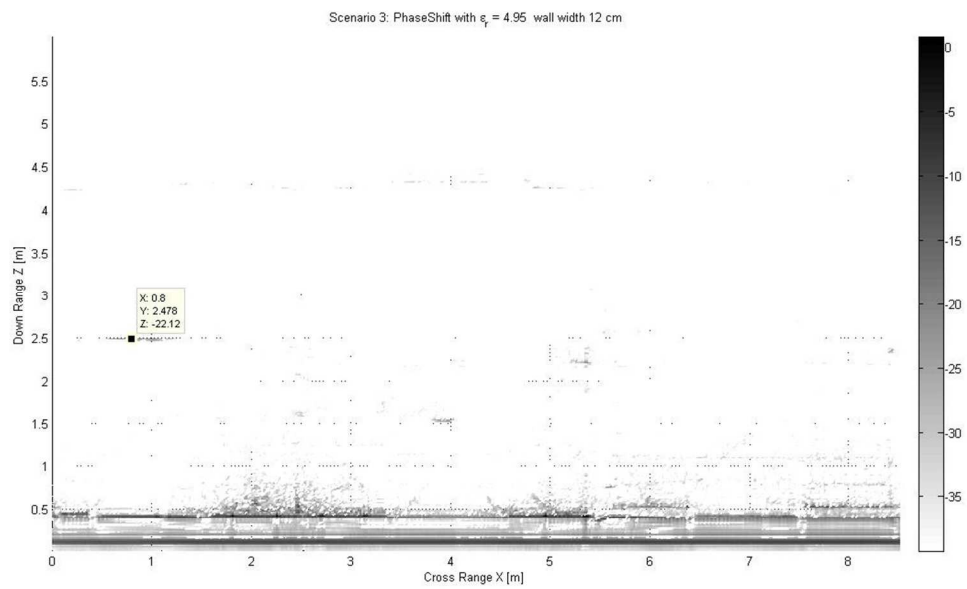


b)

Figure A.: $\epsilon_r = 4.5$, $L_w = 12 \text{ cm}$
 a) Diffraction Stack Result b) Phase-Shift Result



a)



b)

Figure A.: $\epsilon_r = 4.95$, $L_w = 12$ cm
a) Diffraction Stack Result b) Phase-Shift Result

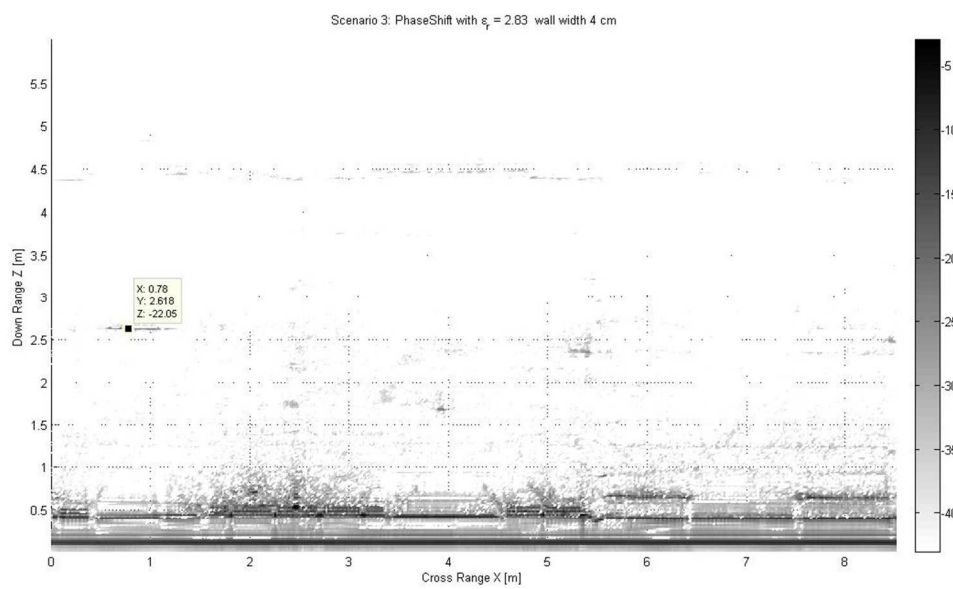
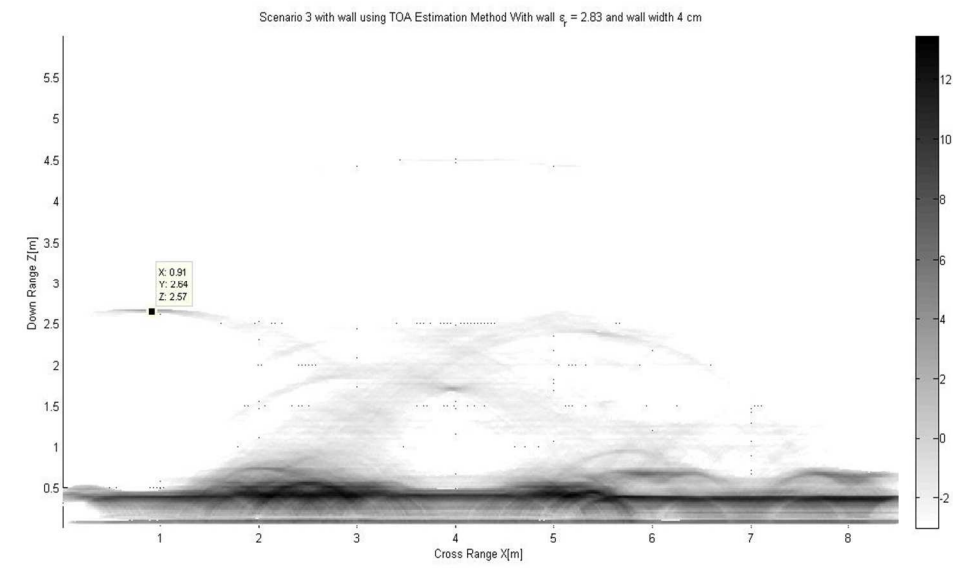


Figure A.: $\epsilon_r = 2.83$, $L_w = 4 \text{ cm}$

a) Diffraction Stack Result b) Phase-Shift Result

References

- [1]. C. Gentile and A. Kik, “A Comprehensive Evaluation of Indoor Ranging Using Ultra-Wideband Technology,” *EURASIP Journal on Wireless Communications and Networking*, vol. 2007, id. 86031, 2007.
- [2]. Zhang, Y.P., and Hwang, Y, “Measurements of the characteristics of indoor penetration loss”. *IEEE 44th Vehicular Technology Conf.*, Vol. 3, pp. 1741–1744, 1994.
- [3]. Andreas F. Molisch, *Wireless Communication*, Wiley Press 2005.
- [4]. S. Gauthier and W. Chamma, “Through-The-Wall Surveillance,” Technical Memorandum DRDC, Ottawa, Oct. 2002.
- [5]. E. M. Johansson and J. E. Mast, “Three-dimensional ground-penetrating radar imaging using synthetic aperture time-domain focusing” *AMMWD, Proceedings of SPIE*, vol. 2275, pp. 205-214, Sep. 1994.
- [6]. I. Immoreev and Fedotov, “Ultra wideband radar systems: advantages and disadvantages,” *Ultra Wideband Systems and Technologies*, pp. 201-205, 2002.
- [7]. I. Nicolaescu, P. Van Genderen, K.W. Van Dongen, J. Van Heijenoort, and P. Haakaart, “Stepped Frequency Continuous Wave Radar-Data Preprocessing,” Workshop on Advanced Ground Penetrating Radar, pp. 177-182, May 2003.
- [8]. H. Hashemi, “The Indoor Radio Propagation Channel,” *Proceedings of the IEEE*, vol. 81, no. 7, pp. 943-968. 1993.
- [9]. Jenö Gazdag and Piero Sguazzero, “Migration of seismic data”. *Proceedings of the IEEE*, Vol. 72, NO. 10, Oct 1984.
- [10]. Chen Lei and Shan Ouyang, “Through-wall Surveillance using Ultra-wideband Short Pulse Radar: Numerical Simulation”. 2nd IEEE Conference on Industrial Electronics and Applications, pp 1551, 24, Sep 2007.
- [11]. M. Dehmollaian, M.Thiel, and K. Sarabandi, “Through-the-wall Imaging Using Differential SAR,” *IEEE Transactions on geoscience and Remote Sensing*, vol. 47, pp. 1289-1296, May 2009.
- [12]. G. F. margrave, “Numerical methods of exploration seismology with algorithms in Matlab,” Master’s thesis, Department of geology and Geophysics, The University of Calgary, Jan. 2001.
- [13]. X. Zhuge, T. G. Savelyev, A. G. Yarovoy , and L. P. Ligthart, “UWBArray-based Radar imaging Using Modified Kirchhoff Migration”, *Proceedings of IEEE Conference on UWB*, vol. 3, 17, Oct. 2008.

- [14]. Jenö Gazdag, “*Wave equation Migration with Phase-Shift method*”, Geophysics, vol. 43. Pp 1342-1351, Dec. 1978.
- [15]. A.J. Braga, C. Gentile, “*An Ultra-Wideband Radar System for Through-the-Wall Imaging Using a Mobile Robot*”, IEEE Communications conference, pp. 1-6, June 2009.
- [16]. Proakis J.G., and Manolakis D.G., *Digital Signal Processing*, Prentice Hall, New Jersey, 1996.
- [17]. A. Muqaibai, A. Safaai-Jazi, A. Bayram, A. Attiya, and S. Riad, “*Ultrawideband through-the-wall propagation,*” *IEEE Proc. Microw. Antennas*, vol. 152, pp. 581–588, Dec. 2005.
- [18]. Y. Yang, A. E. Fathy, “*See-Through-Wall Imaging Using Ultra Wideband Short-Pulse Radar System*”, The ECE Department, University of Tennessee, 2005.
- [19]. C.G. Gilmore, “*A Comparison of Imaging Methods using GPR for Mine Detection and A Preliminary Investigation into the SEM for Identification of Buried Objects*”, Master’s Thesis, University of Manitoba, Canada. Dec 2004.
- [20]. HP 8720C Network Analyzer data sheet
https://www.valuetronics.com/vt/assets/pdfs/HP_8719C_8720C_8722C.PDF